Eur. Phys. J. A (2014) **50**: 47
DOI 10.1140/epja/i2014-14047-4

THE EUROPEAN PHYSICAL JOURNAL A

Review

The FAZIA project in Europe: R&D phase*

The FAZIA Collaboration

R. Bougault[1,a], G. Poggi[2,3], S. Barlini[2,3], B. Borderie[4], G. Casini[3], A. Chbihi[5], N. Le Neindre[1], M. Pârlog[1,6], G. Pasquali[2,3], S. Piantelli[3], Z. Sosin[7], G. Ademard[4], R. Alba[8], A. Anastasio[12], S. Barbey[4], L. Bardelli[2,3], M. Bini[2,3], A. Boiano[12], M. Boisjoli[5], E. Bonnet[5], R. Borcea[6], B. Bougard[1], G. Brulin[4], M. Bruno[16], S. Carboni[2,3], C. Cassese[12], F. Cassese[12], M. Cinausero[10], L. Ciolacu[6], I. Cruceru[6], M. Cruceru[6], B. D'Aquino[12], B. De Fazio[13], M. Degerlier[11], P. Desrues[1], P. Di Meo[12], J.A. Dueñas[9], P. Edelbruck[4], S. Energico[14], M. Falorsi[2], J.D. Frankland[5], E. Galichet[4,21], K. Gasior[18], F. Gramegna[10], R. Giordano[12,15], D. Gruyer[5], A. Grzeszczuk[18], M. Guerzoni[17], H. Hamrita[4], C. Huss[4], M. Kajetanowicz[7], K. Korcyl[20], A. Kordyasz[19], T. Kozik[7], P. Kulig[7], L. Lavergne[4], E. Legouée[1], O. Lopez[1], J. Łukasik[20], C. Maiolino[8], T. Marchi[10], P. Marini[5], I. Martel[9], V. Masone[12], A. Meoli[12], Y. Merrer[1], L. Morelli[16], F. Negoita[6], A. Olmi[3], A. Ordine[12], G. Paduano[12], C. Pain[1], M. Pałka[7], G. Passeggio[12], G. Pastore[2,3], P. Pawłowski[20], M. Petcu[6], H. Petrascu[6], E. Piasecki[19], G. Pontoriere[12], E. Rauly[4], M.F. Rivet[4], R. Rocco[12], E. Rosato[12,13], L. Roscilli[12], E. Scarlini[2], F. Salomon[4], D. Santonocito[8], V. Seredov[4], S. Serra[17], D. Sierpowski[7], G. Spadaccini[12,13], C. Spitaels[5], A.A. Stefanini[2,3], G. Tobia[3], G. Tortone[12], T. Twaróg[7], S. Valdré[2,3], A. Vanzanella[12], E. Vanzanella[12], E. Vient[1], M. Vigilante[12,13], G. Vitiello[12], E. Wanlin[4], A. Wieloch[7], and W. Zipper[18]

[1] LPC Caen, ENSICAEN, Université de Caen, CNRS-IN2P3, F-14050 Caen cedex, France
[2] Dipartimento di Fisica, Università di Firenze, via G.Sansone 1, 50019 Sesto Fiorentino (FI), Italy
[3] INFN Sezione di Firenze, via G.Sansone 1, 50019 Sesto Fiorentino (FI), Italy
[4] Institut de Physique Nucléaire, CNRS/IN2P3, Université Paris-Sud 11, F-91406 Orsay cedex, France
[5] GANIL, CEA/DSM-CNRS/IN2P3, B.P. 5027, F-14076 Caen cedex, France
[6] Horia Hulubei National Institute of Physics and Nuclear Engineering (IFIN-HH), RO-077125 Bucharest Măgurele, Romania
[7] Jagiellonian University, Institute of Physics, ul. Reymonta 4, 30-059 Krakow, Poland
[8] INFN - Laboratori Nazionali del Sud, Via S. Sofia 62, 95125 Catania, Italy
[9] Departamento de Fisica Aplicada, FCCEE Universidad de Huelva, 21071 Huelva, Spain
[10] INFN LNL Legnaro, viale dellUniversità 2, 35020 Legnaro (Padova), Italy
[11] Science and Art Faculty, Physics Department, Nevsehir Haci Bektas University, Nevsehir, Turkey
[12] INFN - Sezione di Napoli, Complesso Universitario di Monte S. Angelo, via Cinthia, 80126 Napoli, Italy
[13] Dipartimento di Fisica, Università di Napoli "Federico II", Complesso Universitario di Monte S. Angelo, via Cinthia, 80126 Napoli, Italy
[14] Istituto SPIN - CNR, Complesso Universitario di Monte S. Angelo, via Cinthia, 80126 Napoli, Italy
[15] Dipartimento di Informatica e Sistemistica, Università di Napoli "Federico II", via Claudio 21, 80125 Napoli, Italy
[16] Dipartimento di Fisica ed Astronomia, Università di Bologna and INFN, Sezione di Bologna, Via Irnerio 46, I-40126 Bologna, Italy
[17] INFN, Sezione di Bologna, Viale Berti Pichat 6/2, I-40127 Bologna, Italy
[18] August Chełlkowski Institute of Physics, University of Silesia, ul. Uniwersytecka 4, 40-007 Katowice, Poland
[19] Heavy Ion Laboratory, University of Warsaw, ul. Pasteura 5A, 02-093 Warsaw, Poland
[20] Institute of Nuclear Physics PAN, ul. Radzikowskiego 152, 31-342 Krakow, Poland
[21] Conservatoire National des Arts et Métiers, F-75141 Paris cedex 03, France

Received: 9 December 2013 / Revised: 3 February 2014
Published online: 27 February 2014 –
Communicated by A. Ramos

Abstract. The goal of the FAZIA Collaboration is the design of a new-generation 4π detector array for heavy-ion collisions with radioactive beams. This article summarizes the main results of the R&D phase, devoted to the search for significant improvements of the techniques for charge and mass identification of reaction products. This was obtained by means of a systematic study of the basic detection module, consisting of two transmission-mounted silicon detectors followed by a CsI(Tl) scintillator. Significant improvements in ΔE-E and pulse-shape techniques were obtained by controlling the doping homogeneity and the cutting angles of silicon and by putting severe constraints on thickness uniformity. Purposely designed digital electronics contributed to identification quality. The issue of possible degradation related to radiation damage of silicon was also addressed. The experimental activity was accompanied by studies on the physics governing signal evolution in silicon. The good identification quality obtained with the prototypes during the R&D phase, allowed us to investigate also some aspects of isospin physics, namely isospin transport and odd-even staggering. Now, after the conclusion of the R&D period, the FAZIA Collaboration has entered the demonstrator phase, with the aim of verifying the applicability of the devised solutions for the realization of a larger-scale experimental set-up.

1 Introduction

The determination of the charge Z and mass A of the particles emitted during heavy-ion collisions is the key issue of any experiment aiming at studying the subject of the symmetry energy. The FAZIA Collaboration was born few years ago, with the goal of improving and extending the techniques, available at that time, of charge and mass identification of ions emitted during heavy-ion collisions at Fermi energies and below. In fact, it was clear that the ΔE-E identification technique was not yet fully implemented and mature, *i.e.* still far from the intrinsic limit determined by the energy straggling. Moreover the new and exciting results [1,2] on the Pulse-Shape Analysis (hereafter PSA) in silicon [3–6] appearing in that period clearly demonstrated the potential of the method. Particularly appealing was the possibility of having low identification thresholds, although the available literature was limited to only few successful examples and rather evidence existed about the non-reproducibility of the method, thus preventing application of PSA to large detector arrays. The root of the FAZIA project is based on expertise gained with existing multi-detectors [7,8]. Furthermore, the emerging and increasingly robust fast sampling techniques applied to nuclear scintillation and semiconductor detectors [9], were expected to successfully extend their application to timing and PSA, promising unprecedented performances. Inside the FAZIA Collaboration it was immediately agreed on the opportunity of defining a first R&D phase (so-called Phase I) dedicated to attack the still open problem of the limits of the ΔE-E identification technique and to better pin down the potential of the emerging PSA technique. A very first effort was dedicated to gather further experimental results, specifically dedicated to understanding the limiting factors of the observed identification results. Once the origin of these limitations was identified and the remedies successfully implemented, the construction of the prototypes of telescopes started and the results confirmed that a real progress in the identification techniques was indeed available and exploitable in view of building a full 4π array.

The present paper is dedicated to the description of the results obtained by FAZIA in its R&D phase. The experiments were performed at *Laboratori Nazionali del Sud* (LNS), *Grand Accélérateur d'Ions Lourds* (GANIL) and *Laboratori Nazionali di Legnaro* (LNL). A large part of the paper is dedicated to a detailed discussion about the main effects determining the Z and A identification properties in silicon detectors, as determined during the R&D phase of the FAZIA Collaboration. In particular experimental results are presented which quantitatively illustrate different effects on both PSA and ΔE-E. It is worth stressing the key role played by the accurate digitization of the signals and by the associated signal processing, which has been proved essential in order to get the best ΔE-E and PSA results. We start, sect. 2, with the description of the FAZIA "recipes" concerning detectors and electronics. Section 3 is dedicated to the presentation of the Z and A identification results obtained by the FAZIA Collaboration with the prototypes of the telescopes having all their characteristics optimized. The Z and A identification quality is described both for the standard ΔE-E and for the PSA techniques. In sect. 4, the issue of the possibly different performances for front and rear injection of the particles in silicon is addressed.

From the very beginning of the R&D phase it has been clear that any progress in the detection and identification techniques should be accompanied, supported and possibly driven by a theoretical analysis of the Physics behind the signal formation in the detectors. During the first R&D period, simulations regarding the signal formation in silicon were developed [10–13] by the Orsay group and L. Bardelli in Florence. In [12] a 3D-simulation without free parameters (see fig. 1) provided important clues of the main physical processes at the basis of the observed signals and their dependence on the detected ion properties (energy, charge and mass). In fact it demonstrated the importance of the electrostatic interaction among charge carriers for the charge collection process. Section 5 presents also another simulation which has been developed in the second part of the R&D phase [14]. Section 6 addresses a

* Contribution to the Topical Issue "Nuclear Symmetry Energy" edited by Bao-An Li, Àngels Ramos, Giuseppe Verde, Isaac Vidaña.

[a] e-mail: bougault@lpccaen.in2p3.fr

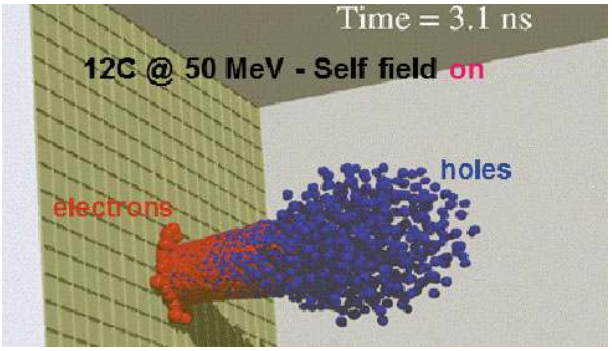

Fig. 1. (Colour on-line) A 3D simulated plasma column for 50 MeV ^{12}C in silicon detector (rear injection). From [12].

few more items which still refer to the activity of the R&D phase of FAZIA, although somewhat aside from its mainstream. Finally, the conclusions provide a general overlook of the FAZIA activity and its future developments.

2 Optimizing Si detector for Z and A identification

The FAZIA Collaboration has carefully evaluated the behavior of signal shapes in silicon detectors in order to find the lower identification energy threshold and the best charge (mass) separation. We started an R&D program based on the optimization of the performances of three-layers 300 μm Si - 500 μm Si - 10 cm CsI(Tl) telescopes. Sizeable improvements have been obtained for both the standard ΔE-E technique and the PSA in each of the silicon stages. Most efforts have been spent on the latter technique for ions which are stopped in the first Si-layer and cannot be identified via the ΔE-E method. Indeed, because of the different stopping powers, different particles with the same kinetic energy produce different energy loss profiles along the detector depth and this results in different charge collection times, *i.e.* in different pulse shapes. As a consequence, using only one detector layer, it is possible to identify in charge (mass) stopped ions by measuring the energy of the stopped reaction product and an additional parameter related to the shape of the charge or current signal. In the present paper, this shape-related parameter is either the rise-time of the charge signal for the "energy *vs.* charge rise-time" method, or the maximum of the current signal for the "energy *vs.* current maximum" method [15].

2.1 Properties of the detectors and electronics

All the silicon detectors are ion implanted of the n-TD type [16], with bulk resistivity values in the range 3000–4000 Ωcm, with an active area of $20 \times 20\,\mathrm{mm}^2$. They are all "transmission mounted", with thin dead layers on both sides and they are manufactured by CANBERRA and FBK. Each of the elements of the FAZIA telescopes (silicon detectors and CsI scintillators coupled to photo-diodes) was connected to custom-designed Front-End Electronics (FEE), consisting of a charge-and-current preamplifier (PACI) [11] followed by sampling ADC's (digitizers). The preamplifiers had different gains and were located near the detectors inside the vacuum chamber. The digitizers were in air, connected to the preamplifiers by differential cables. They were either 125 MS/s 12 bit cards ("Florence" cards [17], developed by INFN-Sezione di Firenze) or 100 MS/s 14 bit cards developed by IPN Orsay, in the framework of the FAZIA Collaboration. The sampled waveforms delivered by the digitizers were then stored on disk and processed off-line in order to extract the relevant parameters for the analysis.

The 14 bit 100 MS/s digitizer boards are mounted as daughterboards on VME motherboards together with the Florence cards. Each board hosts two digitizing channels, one for the charge and one for the current output of a single PACI preamplifier. The input stage, in its most common configuration has the following characteristics:

- Fully differential signal path up to the ADC.
- Anti-aliasing low-pass filter with Bessel response (Sallen & Key circuit configuration) and a cut-off frequency of about 20 MHz. The filter sets a lower threshold of about 20 ns on the rise-time of a digitized signal.
- Overall 6 dB attenuation (a factor of two) to adapt the 4 V peak-to-peak dynamic range of the FAZIA PACI to the 2 V peak-to-peak dynamic range of the ADC's (Linear Technology LTC2254).
- A powerful FPGA (Xilinx Spartan 3) hosting:
  1) the charge and current signal memory (up to 8 kS of total length, with adjustable pre-trigger length of up to 2 kS);
  2) the trigger logic;
  3) a pulse generator/signal monitor for testing (exploiting an on-board digital-to-analog converter);
  4) two digital trapezoidal shapers: a fast shaper (for triggering purposes) and a slow shaper for energy measurements.
- An on-board DSP (Analog Devices ADSP2191) for controlling signal acquisition, compression and transfer to the acquisition system.

On some digitizer boards an alternative method to obtain the current signal was successfully tested: an analog differentiation stage was implemented to obtain the derivative of the charge signal.

The improvement in the identification capabilities presented in this paper is the result of several procedures which were developed during the R&D preparatory phase [18] :

- "Random" cut of the silicon wafers tilted with respect to the major crystal direction. This makes the crystal appear similar to an amorphous material for the incoming particles and reduces the effects related to the crystal orientation [19]. All the silicon wafers of the FAZIA telescopes were cut in this way after demand to the producers (it appeared that nowadays manufacturers do not respect this known rule).

- Usage of silicon detectors with good dopant homogeneity: one starts with highly uniform silicon material obtained with the n-TD process. Control and further selection is then done with a non-destructive laser-based method [20] developed by the Collaboration, that allows to build a map of the resistivity as a function of the position on the silicon. Some detectors with doping inhomogeneities as small as 1% were used.
- Selection of silicon detectors with good planarity and parallelism of front and rear sides, *i.e.* high thickness uniformity.
- Reverse mounting configuration of silicon detectors, so that the particles enter from the low-field side. In this way it is possible to maximize the rise-time differences of the charge signals produced by different stopped nuclei of the same energy [2–5,11,13,21,22].
- An aluminum layer of about 30 nm on both sides of the detectors: this reduces sheet resistance to a level which preserves good timing properties.
- Careful control of the constancy of the electric field inside the detectors as a function of time. In fact, any change of the detector reverse current (which tends to increase with time) induces a change in the voltage drop across the bias resistor (20 MΩ). An accurate monitoring of the current allows for compensation of this drop.
- Usage of dedicated preamplifiers, located inside the vacuum chamber as close as possible to the detector. This is necessary in order to minimize the consequences of the length of the connecting cables on the shape of the signals, on the noise and on the pick-up of disturbances.
- Extensive optimization of the digital treatment of the sampled pulse shapes of both charge and current signals. Digitization is a key issue because numerical treatment of the signals allows for optimal extraction of timing and energy information.

All the listed items contribute to improving Z and A identification. We now focus on some of them.

2.2 Effect of doping non-uniformity

It is well known (see, for example, [1,23,24]) that the PSA performances in silicon are severely influenced by the resistivity non-uniformity of the detector. In particular it has been shown that areas of the detector characterized by different resistivities produce signals having different shapes (*e.g.* different rise-times), thus jeopardizing the achievable performances when the full (*i.e.* non-*ad hoc* collimated) detector area is used. As an example, from the collimated n-TD detector shown in fig. 9 of ref. [25], one sees that the pulse-shape–based isotopic separation between, *e.g.*, ^{12}C and ^{13}C consists of a ~ 0.2 ns difference between the average signal rise-times of the two isotopes. Given the ~ 15 ns average value of the rise-times, this translates into a $\sim 1.3\%$ difference. Therefore, since to a first-order approximation both the transit-time and the plasma time (see, for example, the analytical estimate in [26]) depend linearly on the depletion voltage and hence on resistivity, a given requirement on signals rise-time spread directly translates into a non-uniformity requirement. The presently available quality of off-the-shelf silicon ingots and detectors (about 15%) is thus clearly not adequate and quality-check procedures should at least be employed.

Moreover, despite the technological efforts of the semiconductor industry, presently it is quite difficult to measure (possibly in a non-destructive way) the non-uniformity of a detector at the percent level prior to its operation. It has also to be noted that this quantity may fluctuate widely from one detector batch to another, thus making a sampling-based test quite useless.

With this in mind, the FAZIA Collaboration has developed a non-destructive method for resistivity mapping of silicon detectors [20]. The idea is an extension of the standard Capacitance-Applied Voltage ($C - V_{\rm appl}$) method for detector depletion voltage ($V_{\rm depl}$) or resistivity (ρ) determination by defining a "local" depletion voltage $V_{\rm depl}(x, y)$ as a function of the position (x, y).

A collimated light pulse (or a collimated α-particle source), having very low penetration depth inside silicon, produces a cloud of electrons and holes that are collected by the detector. Only a small part of the detector is involved in this process, namely the volume defined by the source collimation in the (x, y) plane, by the lateral diffusion processes during charge collection and by the detector thickness.

The detector is used in a reverse-mounted configuration, *i.e.* the light pulse enters the detector from the low field side —this means that, when $V_{\rm appl} < V_{\rm depl}$, the carriers are produced in a region of nominally zero electric field.

For a given position (x, y), by examining the collected signals as a function of the applied voltage $V_{\rm appl}$, one expects some "abrupt" change in the signal properties (for example the rise-time) when passing from the regime of non-completely depleted detector to the over-depleted one (*i.e.* absence of any non-depleted region). In analogy with the standard $C - V_{\rm appl}$ method, taking into account that the signal is governed by the properties of the depleted, active volume only, we thus define the "local" depletion voltage $V_{\rm depl}(x, y)$ as the voltage where this abrupt change occurs.

For typical collimations ($\sim$ mm diameter) and detector thicknesses (hundreds of μm) one can approximate the involved active volume as a planar geometry, and thus it is possible to measure the average detector resistivity $\rho(x, y)$ along the z-direction as a function of position (x, y) by application of eq. (1) in [20].

The local depletion voltage can be extracted from a plot of t_{rise} *vs.* $V_{\rm appl}$ (the detector's signal rise-time as a function of the applied voltage) by fitting the experimental points with the function

$$t_{rise}(V_{\rm appl}) = t_0 + a\left(\sqrt{V_{\rm depl}(x,y)} - \sqrt{V_{\rm appl}}\right)^2, \quad (1)$$

where t_0 and a ($a = 0$ for $V_{\rm appl} > V_{\rm depl}(x, y)$) represent the asymptotic rise-time (for $V_{\rm appl} \gg V_{\rm depl}$) and the coef-

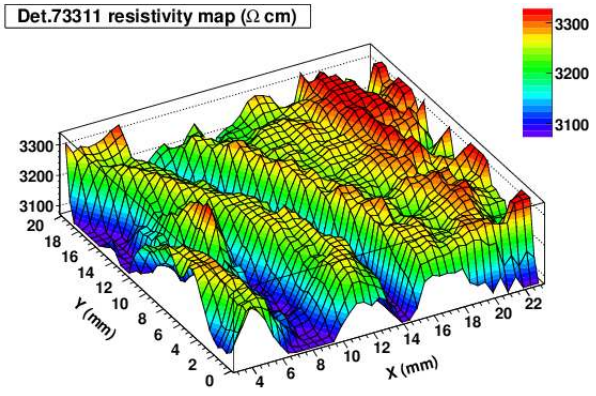

Fig. 2. (Colour on-line) Typical case of an absolute resistivity map obtained with the scanning method developed by FAZIA (a 0.5 mm scanning step has been used). Circular striations in the silicon resistivity are apparent. A non-uniformity of 4.6% has been measured. From [20].

ficient of the behavior apparent for $V_{\rm appl} < V_{\rm depl}$, respectively (see [20] for more details).

Once $V_{\rm depl}(x, y)$ has been extracted for all the scanned positions of the detector it is possible to obtain $\rho(x, y)$, building a bi-dimensional resistivity map of the used detector. In fig. 2 a typical example is shown. The resistivity "landscape" shows the presence of circular structures, or "striations" related to the silicon ingot growing process. Very similar structures are present, with varying importance, in all the tested detectors. While silicon manufacturers usually quote the "maximum-minimum" variation of the resistivity, we prefer the FWHM ($\Delta\rho_{FHWM}$) since it is directly related to the experimental situation where the full active area is used for particle detection (and identification). The value indicated in fig. 2 corresponds to $\Delta\rho_{FHWM}$. As a rule of thumb, we found that typically $\Delta\rho_{\rm max-min} \sim 3 \cdot \Delta\rho_{FHWM}$.

The FAZIA Collaboration decided to focus on n-TD detectors due to their known better resistivity uniformity. Nevertheless, even for n-TD material, non-uniformities ranging from 1 to 6% have been measured. Silicon detectors whose resistivity map had been measured (hence of known resistivity uniformity) have been used to detect nuclear fragments and their PSA capability has been evaluated. We studied the products of the ^{32}S+Al at 474 MeV reaction, thus investigating the particle identification performances of the system over a wide range of charge and mass. Results were obtained using "standard" configurations (ΔE-E Si-Si telescopes and PSA in reverse-mounted [1–3,27] silicon detectors) in realistic operating conditions, in order to better focus on the detector properties and their effects on the final identification performances. The experiment is described in more detail in [18,19]. Here we report, as an example of the effect of doping non-uniformities on PSA identification, the "energy *vs.* charge rise-time" correlations. Data refer to three representative detectors out of the ones tested during the experiment, selecting those that were most similar in terms of used over-bias, thickness (where possible), angle in laboratory, electronic noise and dynamic range, but having different resistivity non-homogeneity. More details on detectors properties are reported in table 1 of [18].

The main effect of resistivity non-homogeneity is a change in the rise-time of the signal as a function of impact position. A proper choice of the shaping time for the energy measurement allows to remove any ballistic deficit effect and thus to avoid any resolution loss in the ΔE-E particle identification. As a consequence only PSA is affected by resistivity inhomogeneity. In fig. 3 the obtained results are shown: the resistivity uniformity improves from left to right, going from $\sim$ 5% FHWM down to $\sim$ 0.7% FHWM, while all the remaining parameters are kept fairly constant. At the time of the experiment we did not have access to a high homogeneity 300 μm detector, so we were forced to use 500 μm ones. The full-range of the used preamplifier+digitizer systems was $\sim$ 4 GeV for all the three detectors. From the picture it is easily seen how the resistivity non-homogeneity plays a key role in the particle identification properties, in particular for particles having small penetration in the detector.

2.3 Effect of crystal orientation

Crystal-orientation related effects play an important role in pulse-height defect, both at low (few MeV [28–31]) and higher energy ($\sim$ 10 MeV/nucleon [32]). The signal shape (*e.g.* rise-time) can also be affected by the orientation of the particle ionization track with respect to the crystal planes, thus spoiling the performance of the PSA technique. The FAZIA Collaboration presented in [19] a first study of this problem. A collimated silicon detector was mounted on a two-axis remotely controlled precision goniometer, which permits to tilt the detector with 0.01 ° steps. The detector orientation was at first aligned using a laser-based alignment system. With this setup, the response of the detector as a function of the direction of the impinging particles with respect to the crystal orientation was explored.

Experiments have been carried out, using ^{80,82}Se at 408 MeV, ^{32}S at 160 MeV and ^{58,60}Ni at 703 MeV beams, elastically scattered by a gold target. Both charge and current signals were acquired and different pulse-shape algorithms applied (charge and current rise-time calculated by using digital constant fraction and deposited energy from the charge signal extracted with digital filtering [33]). In particular one finds that, for ions entering the detector along directions parallel to major crystal planes and/or axes, a sizable increase of fluctuations is present with respect to other directions. Impinging directions far from any crystal axis or plane correspond to minimal fluctuations in energy and rise-time. In the following, they will be referred to as "random" directions, while those with increased fluctuations will be called "channeling" directions. In fig. 4, one can see the difference in the energy and current rise-time distribution of elastically scattered ^{82}Se for a silicon detector manufactured with a $\langle 100 \rangle$ cut in the "channeling" and "random" positions. Using the elastically scattered ^{32}S beam, no significant effect is observed

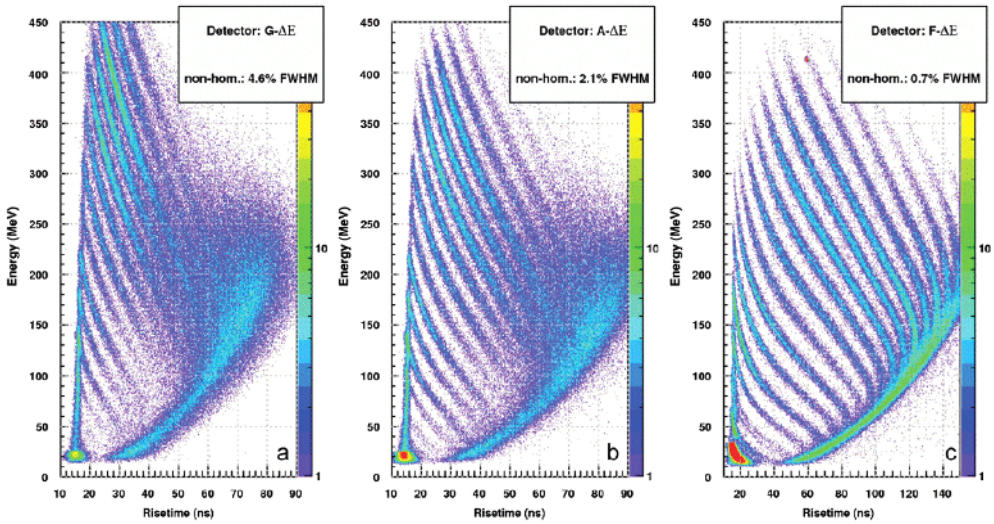

Fig. 3. (Colour on-line) Pulse-shape particle identification plots (energy *vs.* charge rise-time) obtained with three different detectors having different resistivity non-homogeneities (as shown in the insets). See text for details. From [18].

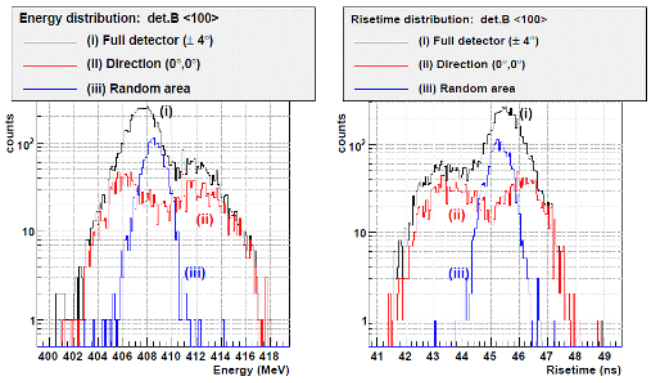

Fig. 4. (Colour on-line) Left: energy distribution for ^{82}Se stopped in a ⟨100⟩ detector. Black histogram (i) refers to full detector, while red histogram (ii) refers to the center of detector ("channeling" position) and blue histogram (iii) to "random" direction. Right: current rise-time distribution for the same detector with the same angular cuts as in the left panel. From [19].

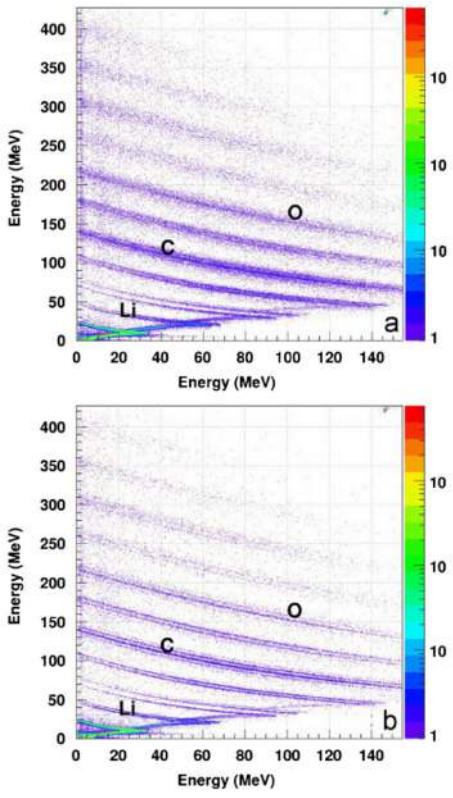

Fig. 5. (Colour on-line) Standard ΔE-E plots obtained with channeled (a) and random configuration (b). From [18].

for the measured energy fluctuations as a function of the rotation angles. This can be ascribed to the much smaller pulse-height defect with respect to the ^{82}Se, which basically prevents any significant effect of the measured energy as a function of crystal orientation. On the contrary, the rise-time is very sensitive to the crystal orientation, even for the ^{32}S beam.

The effect of crystal orientation on identification with PSA in silicon detectors has been studied in [18] exploiting the same projectile-target combination and beam energy cited in the previous paragraph. Several detector and electronics combinations (thickness, preamplifier, sampling) were chosen in order to test various possible solutions and implemented on seven telescope configurations for detecting the products of the reaction ^{32}S+Al at 474 MeV. The detectors have been mounted on a custom designed mechanics that allows to control the orientation of the detectors within $\sim 0.1\,^{\circ}$, as verified with a laser system. Using this mechanics and given the known crystal orientation of the detectors with respect to the support frame, it was possible to tilt the detector at will in order to reach "channeling" or "random" configurations. In fig. 5 the ΔE-E correlation obtained from one of the tested Si-Si telescopes

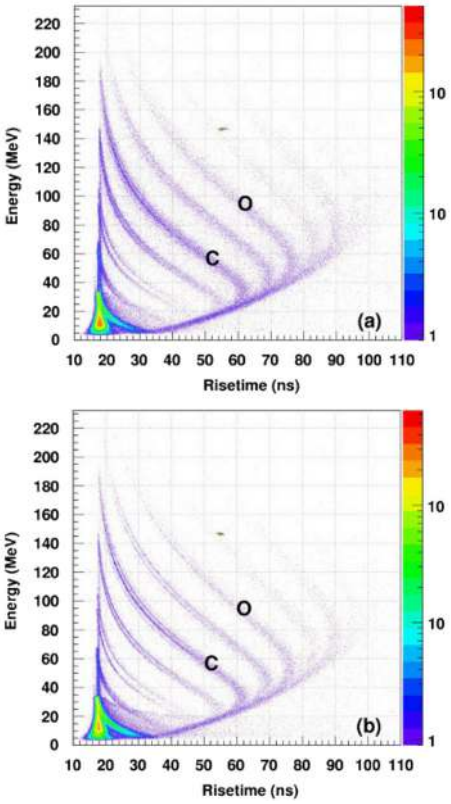

Fig. 6. (Colour on-line) PSA identification via energy *vs.* charge rise-time plots obtained with the detector in channeled (a) and random (b) configuration. From [18].

is shown, both for channeling (a) and random (b) configurations. The full-range of the used preamplifier+digitizer combination was 4.2 GeV for the ΔE detector and 1.3 GeV for the E one. A clear improvement of the particle identification performance can be easily seen in the random orientation, and in particular an important boost of the isotopic separation. In fig. 6 PSA identification via "energy *vs.* charge rise-time" method is shown, again with a comparison between channeling (a) and random (b) configurations. Once again a much better particle identification for the "random" configuration is obtained. This confirms the importance of controlling the channeling effects in PSA applications. In order to minimize orientation-related effects on PSA, FAZIA Si detectors are now produced from wafers cut from the ingots at carefully chosen angles with respect to the ingot axis.

3 PSA and ΔE-E identification results

Identification results (ΔE-E and PSA) are now presented using what could be termed "the FAZIA recipes", as listed in the preceding section.

A 35 MeV/nucleon ^{129}Xe beam was used for bombarding thin targets of ^{nat}Ni and Au. All results presented in this section refer to the reaction products obtained by adding up the data of both reactions, in order to obtain larger statistics.

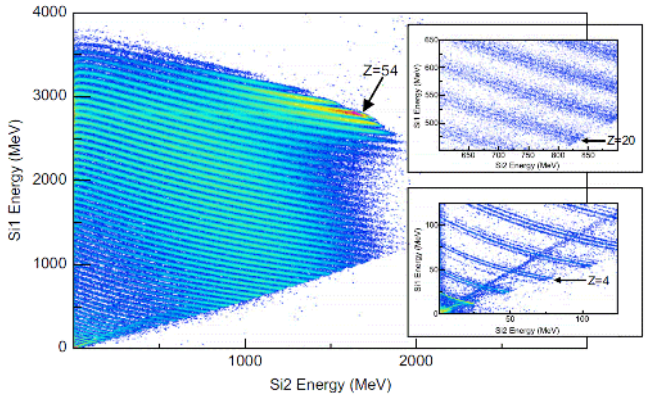

Fig. 7. (Colour on-line) ΔE-E correlation using two 300 μm silicon detectors. The two insets are expansions around $Z = 4$ and $Z = 20$. From [15].

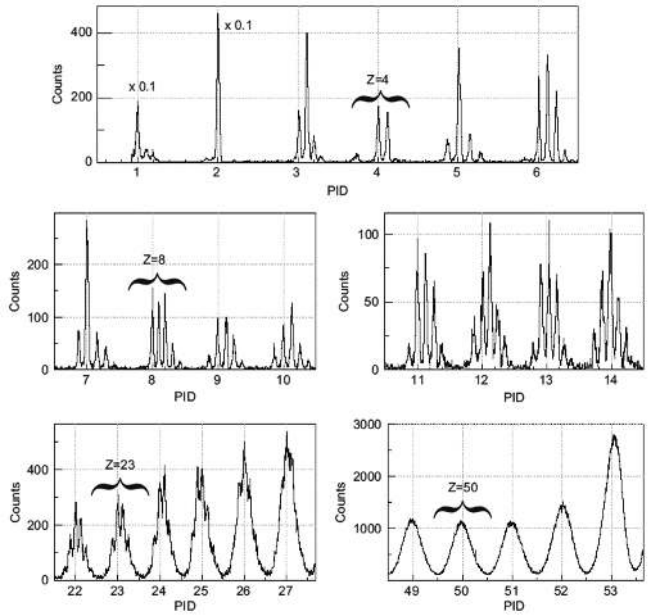

Fig. 8. Distributions of the PID parameter obtained for the data of fig. 7. From [15].

3.1 ΔE-E identification method

The ΔE-E technique is based on the measurement of the energies deposited in two detectors. Therefore, to be identified a particle should at least punch through one detector layer. As FAZIA consists of Si1(300 μm)-Si2(500 μm)-CsI(10 cm) telescopes, two ΔE-E matrices can be drawn using the energy of the impinging nuclei: Si1-Si2 for ions stopped in the Si2 or (Si1+Si2)-CsI for those reaching the CsI.

In fig. 7 the ΔE-E correlation for Si1-Si2 is presented for particles stopped in Si2 (in this case a 300 μm n-TD silicon detector). Charge identification for all ions produced in the collisions, from hydrogen to xenon ions, are clearly visible. The two insets in fig. 7 are expansions for light particles and intermediate mass fragments, respectively.

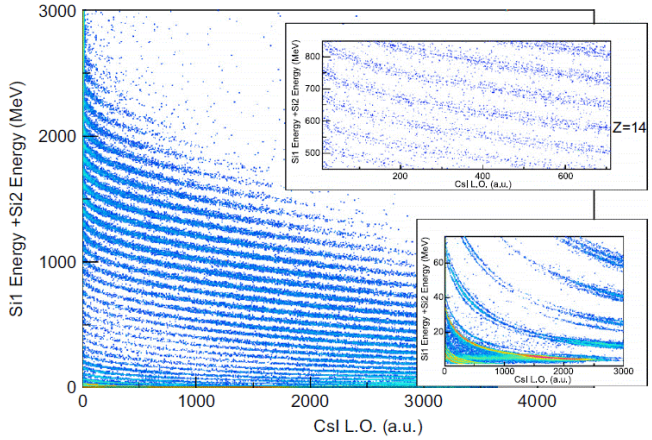

Fig. 9. (Colour on-line) ΔE-E correlation using the summed energy information (Si1+Si2) of the two 300 μm silicon detectors *vs.* the Light Output (LO) of the rear CsI. The insets present two expansions around $Z = 2$–6 and 12–16. From [15].

For particle identification a standard linearization procedure was applied to the ΔE-E correlation of fig. 7. Then the Particle IDentification (PID) parameter was obtained with a linear interpolation between adjacent Z-lines. The histograms of fig. 8 show the distributions of PID integrated over the whole energy range explored by the correlation of fig. 7. Clear mass resolution is obtained up to $Z \simeq 26$.

The ΔE-E correlation for particles stopped in the CsI is shown in fig. 9.

In this case the two energies (Si1 and Si2) were summed up to build the ΔE-E plot while the residual energy E is obtained by the light output in the CsI. Elements are fully identified over the whole dynamic range. The correlation of fig. 9 has been linearized and projected to obtain the PID spectra shown in fig. 10.

A reasonable isotopic resolution is visible for pairs of isotopes of $Z \leq 26$.

One may wonder whether our identification capability has arrived close to the physical limit imposed by energy straggling. In fact, the unavoidable fluctuations caused by energy straggling processes contribute to the overall resolutions of the measured ΔE and E, and hence also to the overlap of the PID-distributions for neighbouring ions. The comparison with simulations (like pure Bohr straggling [15] for instance) indicates that the achieved PID resolution is quite close (within 20%) to the physical limit imposed by the straggling phenomena.

3.2 Pulse-shape identification method

As the PSA methods require information from only one detector, all results presented in this section have been obtained with a veto condition on the detectors behind. In order to have large dynamic ranges, low amplification values were used in the present experiment. A consequence of this choice was that no isotopic resolution with PSA could

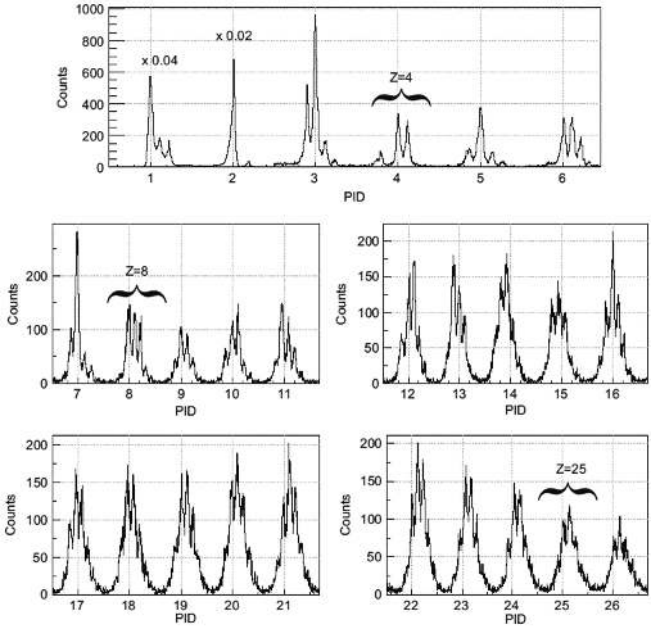

Fig. 10. Particle IDentification (PID) spectra obtained with the data of fig. 9. From [15].

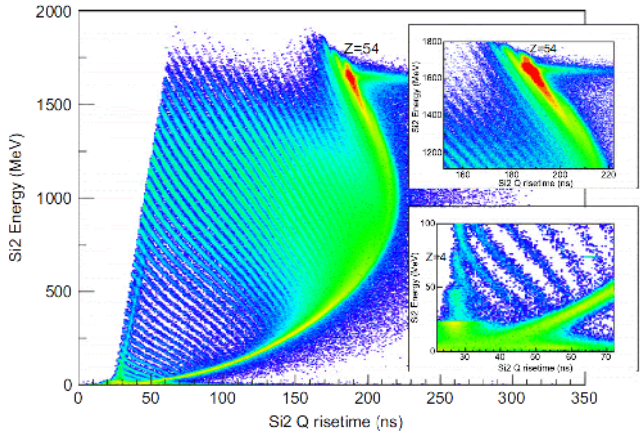

Fig. 11. (Colour on-line) Left: correlation energy *vs.* charge rise-time for nuclei stopped in the second 300 μm silicon detector. The intensity is in logarithmic scale. Right: expansions in the region of the lightest particles and in the region of the elastic scattering. From [15].

be observed, at variance with other FAZIA experiments using higher amplifications [18,19] as shown in fig. 6.

In fig. 11, the correlation "energy *vs.* charge rise-time" is presented for the second silicon detector of a FAZIA telescope. The high intensity area in the upper right part of the figure corresponds to (quasi)-elastically scattered Xe nuclei. Adjacent elements, indicated by the ridges of the correlation, are separated up to the maximum value of $Z = 54$. The left end of the identification ridges corresponds to particles traveling through the whole thickness of the detector. At the opposite end, corresponding to large rise-times, a kind of back-bending is clearly visible. With decreasing energy, the rise-time increases un-

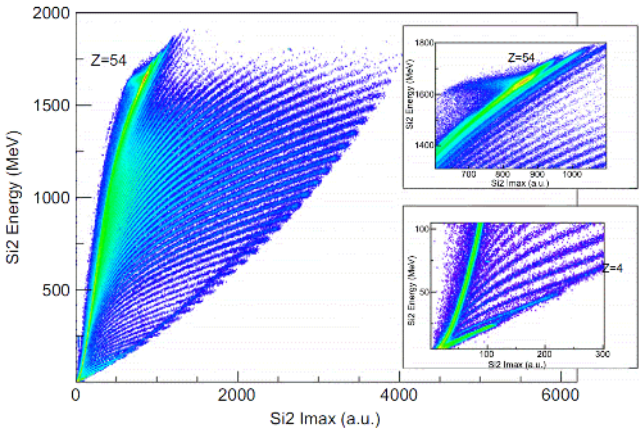

Fig. 12. (Colour on-line) Same as fig. 11, but for the correlation energy *vs.* current maximum. From [15].

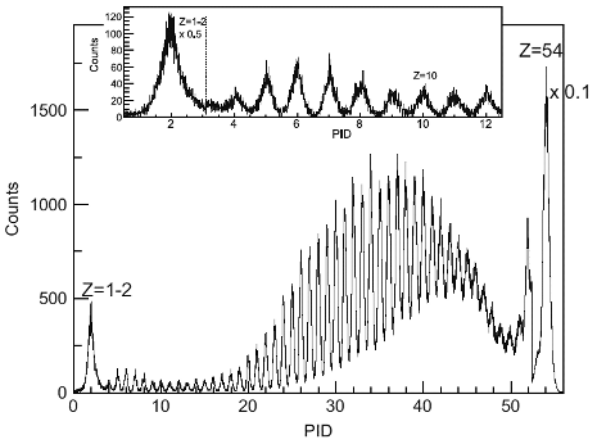

Fig. 13. Particle identification with the energy *vs.* charge rise-time technique, obtained from the linearization of fig. 11. The inset shows an expansion for the light elements. From [15].

til all ridges merge into the very intense quasi-parabolic structure on the right, but from this point on, the rise-time decreases with decreasing energy. It corresponds to ions penetrating only several tens of micrometers into the detector, the exact value depending on Z. This is a typical feature of the correlation produced with reverse mounted silicon detectors and represents the low-energy threshold for particle identification with this kind of PSA [1,2].

The "energy *vs.* current maximum" correlation is shown in fig. 12 for the same data as in fig. 11. Also with this method fragments are resolved in charge over the whole range of Z. In this correlation, particles traveling through almost the whole detector are located at the right end of the ridges, particles stopped just after entering the detector merge together in the almost vertical structure on the left.

The charge separations obtained with both techniques can be appreciated from figs. 13 and 14.

They show the PID histograms obtained from the linearization of the ridges of figs. 11 and 12, respectively. A graphical cut has been employed to exclude the region

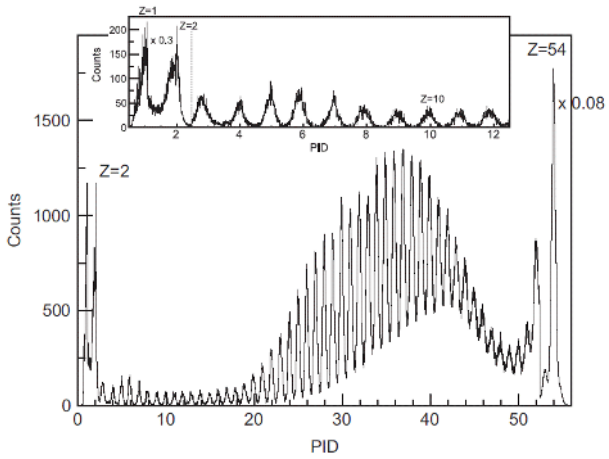

Fig. 14. Particle identification with the energy *vs.* current maximum technique, obtained from the linearization of fig. 12. The inset shows an expansion for the light elements. From [15].

where all the ridges merge (*i.e.* particles stopped near the entrance side of the detector).

3.3 Lowering the energy thresholds of identification with PSA

In a real experiment the pulse-shape analysis technique will be used to identify weakly penetrating particles stopped in the first detector. It is thus interesting to compare the charge-identification energy thresholds obtained for PSA, with those expected for the conventional ΔE-E technique. We need a quantitative way to estimate the PSA identification thresholds. Therefore we apply the "Figure of Merit" (FoM) protocol [34] for adjacent peaks in the particle identification spectra. The FoM is defined as

$$\mathrm{FoM} = \frac{|\mu_1 - \mu_2|}{(\sigma_1 + \sigma_2) * 2.35}, \qquad (2)$$

where μ_1 and μ_2 are the centroids, σ_1 and σ_2 the standard deviations of two Gaussians fitted to adjacent peaks. A value of FoM = 0.7 was conventionally chosen in order to extract a low-energy threshold above which we realize a good identification. The same value FoM = 0.7 leads to different energy thresholds of identification for ejectiles differing by one charge unit for the whole Z domain. For the ΔE-E technique, the threshold is simply the energy necessary to pass through the whole thickness (300 μm) of the first silicon detector.

The plot of fig. 15 shows the sizable lowering of the energy threshold which can be obtained by employing PSA techniques on the first silicon detector (full red points for "energy *vs.* charge rise-time" method and open blue squares for "energy *vs.* current maximum" method) with respect to the more conventional ΔE-E technique (black triangles). On the left part of fig. 15, the thresholds are expressed in terms of the total energy, on the right part in terms of energy per nucleon (for heavy nuclei, the mass has been estimated with the formula

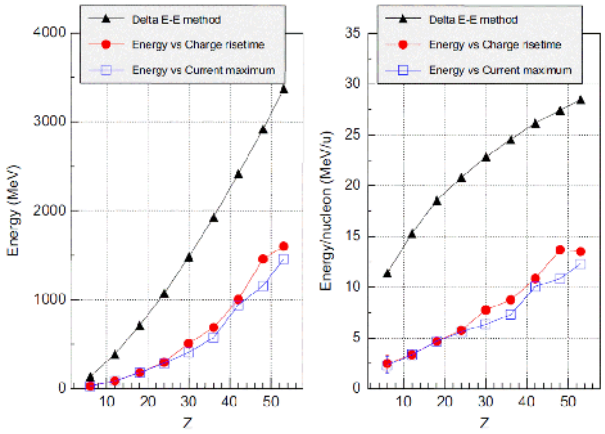

Fig. 15. (Colour on-line) Energy thresholds for Z identification with ΔE-E (first layer of 300 μm) technique (black triangles) and with PSA techniques (red points and blue squares) as a function of atomic number Z. The thresholds values are presented in terms of total energy (left) and energy per nucleon (right). From [15].

$A = 2.08 \times Z + 0.0029 \times Z^2$, see [35]). For example, for nuclei around calcium, the use of PSA in the first silicon detector allows to separate different elements already at kinetic energies of about 6 MeV/nucleon. With the ΔE-E technique, the requirement of passing the first detector introduces a threshold of about 20 MeV/nucleon. The thresholds obtained for the PSA correspond to ranges in silicon of $\simeq 30\,\mu$m for $Z \simeq 6$ and of $\simeq 100\,\mu$m for $Z \simeq 48$. Obviously, the thresholds of the ΔE-E technique could be reduced by employing thinner ΔE detectors. However, to compete with the PSA, very thin ΔE detectors are needed, which would have drawbacks for what concerns thickness uniformity, energy straggling and electronic noise.

3.4 Effect of radiation damage

Having obtained very promising results from PSA using detectors of controlled doping uniformity and orientation, the robustness of detector performance for prolonged exposure to the impinging radiation had to be evaluated and tested in view of long experimental campaigns. In heavy-ion collision experiments, the major source of damage in silicon detectors is the loss of ion kinetic energy via nuclear interactions with lattice atoms. Qualitatively, the incident particles interact with silicon atoms which are displaced from the crystal lattice. Each displacement can generate stable lattice defects, for instance Frenkel pairs, made of a silicon interstitial and the corresponding vacancy. Low-energy recoils are expected to produce just fixed point defects, while energetic recoils could create a dense agglomeration of defects at the end of the primary ion track. Displacements can manifest themselves as energy levels in the band-gap of the silicon crystal, resulting in increase of reverse current, charge trapping and change in the internal electric field. In a way or another all these effects may alter the charge and current signal shapes thus spoiling the PSA identification performance of the detector.

During a test, the FAZIA Collaboration has studied the behavior of detectors irradiated by reaction products and elastically scattered ions from the reactions ^{129}Xe + $^{\rm nat}$Ni and ^{129}Xe + ^{120}Sn at 35 MeV/nucleon [36]. The observed changes in detected signal shapes and their consequences on the related physical observables (energy and charge rise-time) have been described without attempting an explanation in terms of microscopic models of radiation damage. The response of a silicon detector exposed to elastically scattered beam particles (hereafter named "RD" detector) was studied as a function of the irradiating fluence, recording signals coming from three different regions: a region where elastically scattered beam particles were first degraded in energy to 14 MeV/nucleon by a 300 μm silicon absorber, then stopped inside the detector ("stopping zone" in the following), a region where they punched-through it ("transmission zone") and a region not exposed to heavy fluxes of beam particles ("no damage zone"). Each region was defined by a circular collimator of 3 mm diameter. In addition a three-stage FAZIA telescope ("TeleA" in the text) was mounted close to the grazing angle, as in a "real-life" nuclear experiment. TeleA received a quite lower fluence of both elastically scattered Xe-ions and reaction products with respect to the RD detector. In TeleA the effects of radiation damages for ions stopped in the second silicon stage have been studied, focusing on the PSA capability. A detailed description of the setup and of the irradiation cycle can be found in [36]. Here we will briefly discuss the main results obtained regarding the signal shape, because they are most relevant for PSA identification. For the stopping zone of the RD detector a substantial decrease of the collected charge for elastically scattered Xe-ions with increasing fluence (-16% at the final fluence of 6×10^8 ions/cm^2) was noticed. The effect is probably due to recombination of electrons and holes at trapping defect sites, where they can exploit the presence of energy levels in the forbidden band. The transmission zone also showed a slight decrease of about 2%. The charge collection time (*i.e.* the rise-time of the charge signal) was also found to decrease with fluence. In fig. 16 both the aforementioned effects, reduction of charge signal amplitude and rise-time are clearly visible for the stopping zone (right panel). Also a slight variation of signal shapes for punching through Xe ions is observed (left panel). Actually, for the "transmission" zone the charge rise-time is diminishing during the measurement by 5%. No significant changes for the same fluence are observed for the "no damage" zone, compared to the "transmission" zone.

TeleA gives us some hints about the possible performances of a FAZIA telescope in a configuration similar to a real physics experiment. The standard PSA plots "energy *versus* charge rise-time" obtained from TeleA at the beginning and at the end of the experiment were found sensibly different. In particular the quality of the fragment identification became much worse with increasing fluence. To be more quantitative, we have linearized the correlations obtained at different fluence values by calculating,

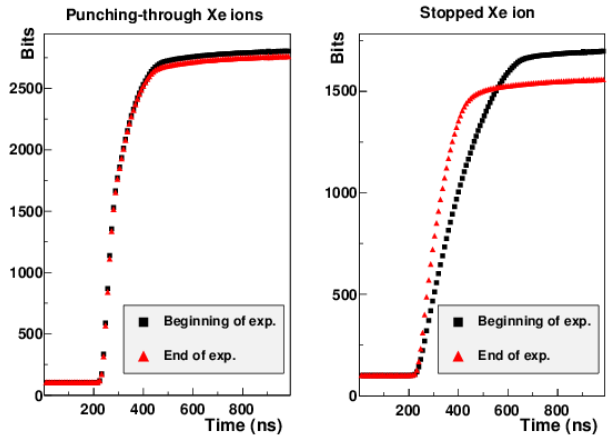

Fig. 16. (Colour on-line) Average charge signal shapes of one thousand ^{129}Xe ions punching through (left panel) or stopped in the silicon (right panel) at the beginning (squares) and at the end (triangles) of the experiment. From [36].

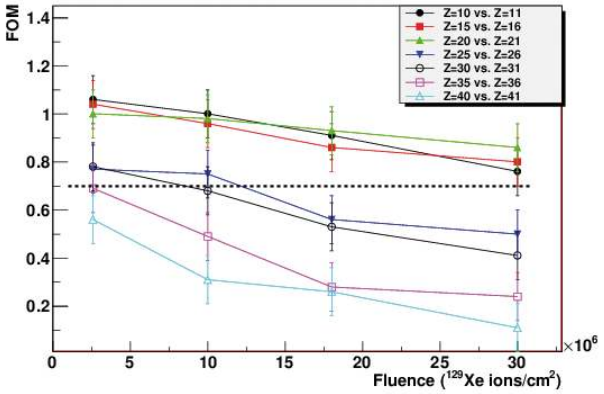

Fig. 17. (Colour on-line) Figure of Merit obtained from the PID spectra for different adjacent elements as a function of the xenon ion beam fluence. From [36].

for each event, a PID parameter. Element separation can then be quantified by calculating a FoM. The FoM behaviour between different adjacent elements as a function of the fluence is reported in fig. 17. Considering that the most important contribution to the overall fluence is that of the elastically scattered ^{129}Xe ions and that not the total surface of the detector was below the grazing angle, an effective area had to be employed in fluence calculations. The acquisition dead time was also taken into account in calculating the fluence (at variance with the RD detector, connected to dedicated scalers for counting the impinging particles). As before, FoM = 0.7 (dotted horizontal line in fig. 17) is used as a reference threshold above which we assume a good peak separation. Though at the beginning of the experiment ions with $Z < 30$ are well separated, the FoM values clearly decrease with increasing fluence so that the identification limit is satisfied only for $Z \leq 20$ at the end of the irradiation. Considering 1% for the relative variation of both the energy and charge rise-time as the maximum acceptable variation for good PSA performance, we fixed the corresponding maximum fluences for stopped and traversing Xe ions to 1×10^7 and 3×10^8 particles/cm^2, respectively. These limits are also compatible with the TeleA results, summarized in fig. 17. A strong dependence of these values on the charge of the stopped ion is expected, and some annealing procedure with heating cycles can be tested in the future in order to (partially) recover the most damaged silicon detectors.

4 Comparison of rear and front side particle injection

The aim of the present section is to compare PSA techniques for front and rear side particle injection. Indeed, the shape of the signals is very sensitive to the strength and the configuration of the electric field inside the detector. Therefore, as expected, we observed a different behavior when nuclear products enter the silicon n-p junction through the front side with the high electric field or through the rear side with the low electric field. In the front configuration the signals are faster and rise-times are less different for different particles and energies. Therefore this configuration presents a priori a big advantage if one wants to perform also a time-of-flight (tof) measurement. This solution, adopted in [37], implies some spoiling of PSA and therefore a compromise should be found.

For a specified ion, the shape of the induced signal depends not only on the specific rate of energy loss and on the electric field, but also on the detector capacitance, preamplifier characteristics and anti-aliasing filter. Using exactly the same detector and electronics for particles incident on the front or rear side should provide a better understanding of the signal shapes. This allows a fair comparison exactly in the same conditions, including reaction product distributions. PSA correlations and their qualities in terms of energy thresholds and shapes have been investigated [22]. Fragments produced in nuclear reactions ^{84}Kr + ^{120,124}Sn at 35 MeV/nucleon, have been used to compare both situations as well as various ion identification techniques like ΔE-E and PSA. During the first part of the experiment, particles impinged on the detectors through the high electric field side (front side injection) for both silicons (Si1 and Si2) of the telescope. Then for the second half of the experiment, both the Si1 and Si2 were turned by 180 °.

4.1 ΔE-E identification technique

It has been established that for the standard ΔE-E technique (particles punching through the first silicon and stopped in the second one) no significant variations of the identification capability between both configurations have been observed. A very good charge separation for all incident particles as well as an equal impressive isotopic discrimination up to $Z = 23$ have been obtained with the very same good quality criteria [22].

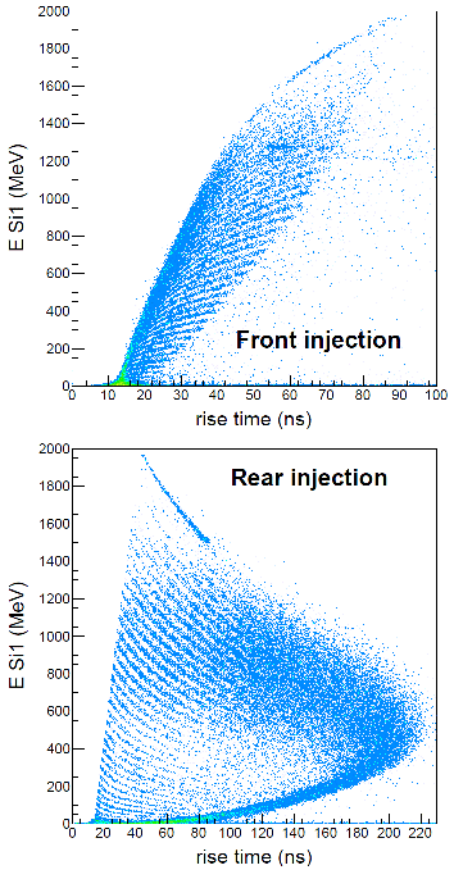

Fig. 18. (Colour on-line) PSA technique: Energy *vs.* rise-time of the charge signal for particles stopped in the first silicon (Si1). Particles punching through the detector have been removed. From [22].

4.2 Pulse-shape identification technique

For the front side injection configuration, the correlation between the energy and the maximum of the current signal (Imax) does not give any visible identification. All elements merge together in a very compact cloud, corresponding to a strong correlation between the energy and the maximum current. Thus the maximum amplitude of the current signal is not a good PSA variable when the fragments enter through the high electric field side. Regarding the "energy *vs.* charge rise-time" correlations shown in fig. 18, we obtain in both cases identification maps, although, the shape of the correlation is very different in the two cases. For the front side injection, the charge rise-time continuously decreases with decreasing energy for ions of any Z value. On the contrary, for rear side injection we observe, for a given Z and starting from high kinetic energies, a rise-and-fall trend of the rise-time. For slow ions, this rise-and-fall produces a ridge where all Z values merge together, whatever the particle is. In both cases a no-identification zone is visible for each line at low energy, defining a Z dependent identification threshold. These thresholds will be determined more precisely in the following.

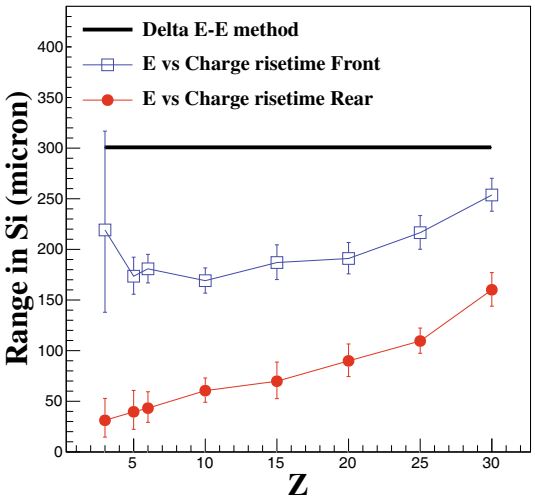

Fig. 19. (Colour on-line) Thresholds expressed in term of range in silicon material for Z identification with ΔE (300 μm)-E technique (black thick line) and with PSA technique (energy *vs.* charge rise-time: red points are for rear side injection and blue squares for front side injection) as a function of atomic number Z. Error bars take into account the statistic and the FoM method reproducibility to extract the energy thresholds. From [22].

4.3 Particle identification thresholds for rear and front configuration

At first sight, the rear side injection method may seem more efficient, since it enlarges the ridge range. However the quantitative FoM method was applied to both matrices of fig. 18 in order to judge the identification quality for both configurations. The FoM = 0.7 identification limit criterion was again adopted. The identification thresholds are summarized in fig. 19 in terms of the range in silicon, where a spectacular improvement on the identification energy threshold for the rear side injection technique is observed (red line and full symbols). For the front side injection case the range for identification varies from a minimum of 170 μm to about 250 μm, whereas in the rear side injection case the minimum range presents a continuous increase, from 30 to 150 μm. The detector performances, in terms of identification thresholds, depend on doping homogeneity. Somehow higher threshold values are reported here for rear injection as compared to results of sect. 3, because the detector used for the rear-front comparison had a worse homogeneity.

5 Simulation and study of signals generated by charged particles in silicon detectors

The high frequency sampling of the current or charge signals gives access to their shape *versus* time. The signals generated by heavy ions have a longer duration as compared to those corresponding to light particles (like protons), due to a slower charge carrier collection —the plasma delay phenomenon [3,38]. The dependence of this

shape on the nature (Z, A, E) of the impinging particle via the specific rate of energy loss became one of the runways used for the heavy-ion identification in the framework of the FAZIA Collaboration. The description of the signal shape by realistic simulations will hopefully provide automatic procedures of calibration and nuclear fragment identification in large scale arrays, provided that the preamplifier transfer function is known [11]. Microscopic approaches [12,14] give insight on the screening due to the high bulk concentration of the generated charge carriers and on their transport; however they require large computing times. To circumvent this obstacle, phenomenological approaches have been also conducted [13].

5.1 Quasi-microscopic treatment

The model [14] is in some respect an extension of that shown in [12]. It uses Gaussian clouds for carrier propagation representation. The propagation is done in the effective electric field determined by both the static voltage applied to the detector electrodes and by the Coulomb interaction between the Gaussian charge clouds. They are introduced to handle large number of carriers creating a complex multi-body system and to conduct some analytical calculations. Gaussian centroids are ruled by drift, and Gaussian variances are influenced by diffusion and drift. The propagation of carriers is performed in both directions, parallel and perpendicular to the primary ionization path. For the calculation, physical coefficients describing the effective electric field propagation, the drift and diffusion processes in silicon are used. As mentioned in [14] only one coefficient is a free parameter for the description of the plasma delay effect, the electron variance mobility, $\mu_{\sigma e}$, related to the evolution of the Gaussian variance. It was set to 2 $\frac{\mu m^2}{Vns}$ (about 1.5% of mobility) and the holes variance mobility is deduced by the following model assumption:

$$\mu_{\sigma h} = \mu_{\sigma e} \frac{\mu_{xh}}{\mu_{xe}}, \tag{3}$$

where electron mobility (μ_{xe}) and holes mobility (μ_{xh}) are material constants.

The reverse detector configuration (rear) is investigated by the model because it gives better results for PSA method (see fig. 18). The data description is reasonably successful for current signals (see fig. 7 of [14]) and the collection time found in the model is strongly correlated to the experimental total current time signal (i.e charge rise-time). We present in fig. 20 the model prediction for element identification. One can notice typical experimental shapes with back-bending at lower energies. That point is of high importance as below that level the identification ability of PSA method is lost. It should be noted that the calculation was performed according to the experimental conditions of ref. [11]; an identification threshold of about 30 MeV is found for carbon, a value compatible with experimental results given in fig. 15 for another silicon detector. In fig. 21 a calculation for different carbon isotopes (^{10,12,14}C) is presented. Isotope separation is qualitatively

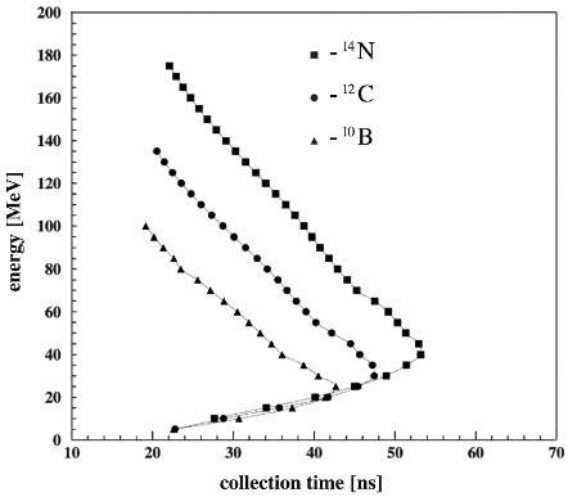

Fig. 20. Model calculation for three elements: energy *versus* collection time identification matrix. From [14].

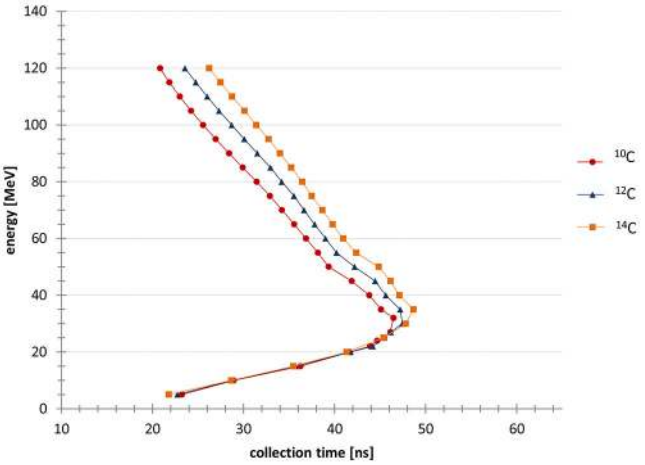

Fig. 21. (Colour on-line) Model calculation for even mass carbon isotopes ^{10}C, ^{12}C, ^{14}C: energy *versus* collection time identification matrix.

obtained above the mentioned back-bending line, proving that with adequate experimental conditions (signal amplification and FAZIA recipes previously mentioned) one may expect mass identification for light fragments with PSA as obtained in fig. 6.

5.2 Phenomenological treatment

Alternatively to the previous approach, we have developed a phenomenological charge carrier collection treatment [13], which considers the progressive extraction of the electrons and holes from the high carrier density zone along the ionizing particle track. This region is assumed to present a supplementary dielectric polarization and consequently a disturbed electric field [39]. Figure 22 presents the exact coordinate dependence of the modified electric field for reverse configuration (inside and outside the 80 MeV ^{12}C ion range - 131 μm), which is found as the solution of the one dimensional Maxwell's equation for the

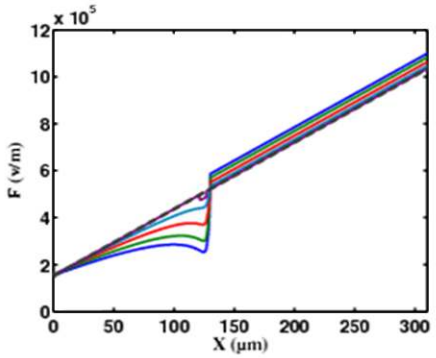

Fig. 22. (Colour on-line) The distorted electric field strength inside the silicon detector, at different times, due to the ionized column induced by 80 MeV ^{12}C ions penetrating on the rear side ($x = 0$ at the rear side contact). The straight dashed line gives the undisturbed electric field. Each continuous line represents the distorted field at different 5 ns time steps (see the text for explanation). From [13].

electric field in this inhomogeneous medium. The largest difference with respect to the undisturbed field (dashed line) is observed for time = 0 (the ionization time) while the other curves are in steps of 5 ns. The parameter relating the modified permittivity to the local instantaneous carrier linear density is one of the two important parameters of a χ^2 minimization procedure used to reproduce the current signals induced by the incoming heavy ions.

The second essential parameter is the dissociation probability of the electron-hole pairs, while the third one, compatible with zero, is the linear-density threshold below which the controlled extraction of carriers stops. The current signals of 10 different heavy-ion species at known energies around 10 MeV/nucleon [40] were satisfactorily described by the fit procedure based on our formalism (six examples are shown in fig. 23). For a given detector and bias voltage, the experimental pattern is sensitive to the nature of the incident charged particle. The values of the two main fit parameters depend, in a rather predictable way, on the specific rate of energy loss too [40]. It is interesting to include their behavior in the driving equations in order to get expressions depending on constant coefficients, independent of the type and energy of the particles. They would be obtained in a second step by means of a global fit procedure, simultaneously applied to a large number of ions at different energies, providing thus a rapid automatic method for ion identification and energy calibration.

6 Alternative technical solutions

6.1 Under-depleted silicon detectors

In a recent test, we have explored the identification capabilities of reverse mounted partially depleted detectors. In such a configuration, the fragments enter the detector through an undepleted region, where the electric field is

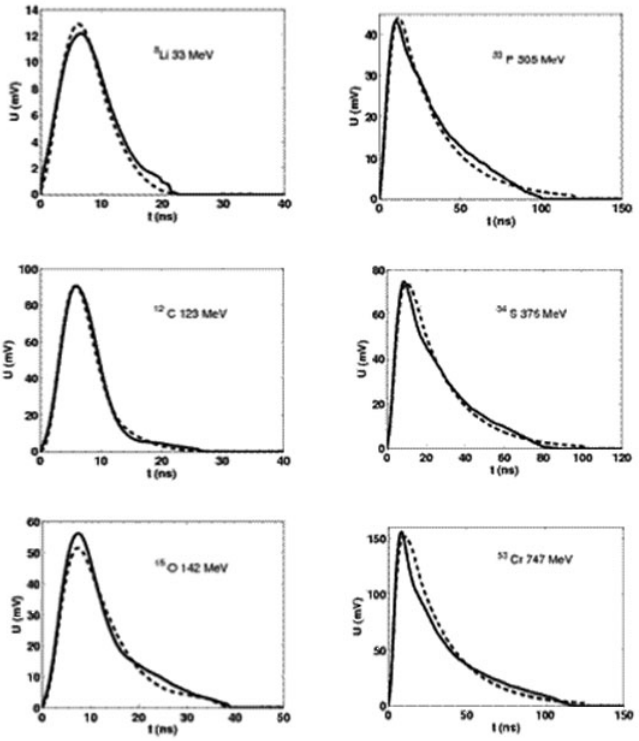

Fig. 23. Simulated signals (dashed curves) compared with the experimental ones (solid curves) for different ions and energies. From [40].

nominally zero. A detailed analysis of this study case, including a study of charge collection efficiency and energy calibration, will be published in a forthcoming paper [41]. In the following we will focus on PSA via the "energy *vs.* current maximum" method, since for partially depleted detectors it shows the most promising results.

In fig. 24 "energy *vs.* current maximum" correlations are shown for different bias voltages applied to a 500 μm thick Si2 stage. The full depletion voltage is 290 V. An improvement of isotopic separation, above the identification energy thresholds, with decreasing bias voltage can be clearly spotted in the figure. Therefore the better mass resolution capability comes at the price of higher identification energy thresholds. Visual inspection of fig. 24 permits to evaluate the identification energy thresholds for different elements, reported as a function of Z in fig. 25.

From fig. 24 it is apparent that at 105 V and 130 V bias voltages the energy thresholds for charge identification are only slightly lower than those for mass identification.

We would like to stress that the detector under test did not allow isotopic identification via PSA when biased at full depletion voltage. In fact its doping uniformity is only about 6%, while previous tests performed by the Collaboration showed that a doping uniformity of about 1% FWHM or less is needed for isotopic identification [18]. On the other hand, when not fully depleted, PSA of detector signals allowed for both charge and mass separation of fragments, though charge identification energy thresholds were higher than at full depletion.

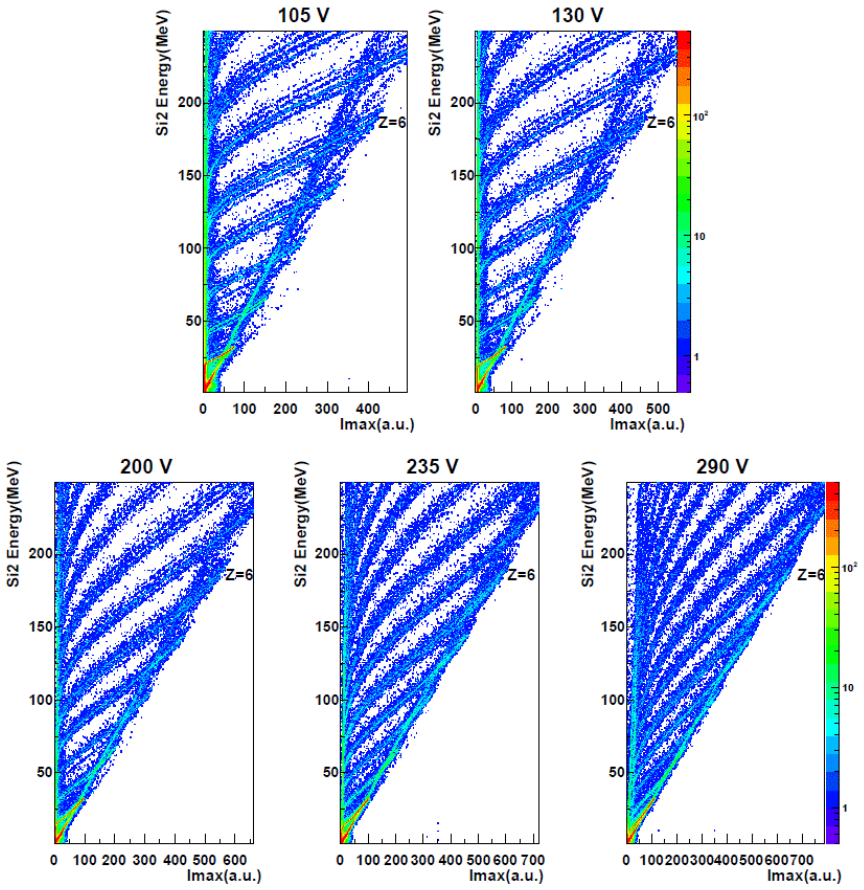

Fig. 24. (Colour on-line) Energy *versus* Current maximum correlations at different bias voltages. From [41,42].

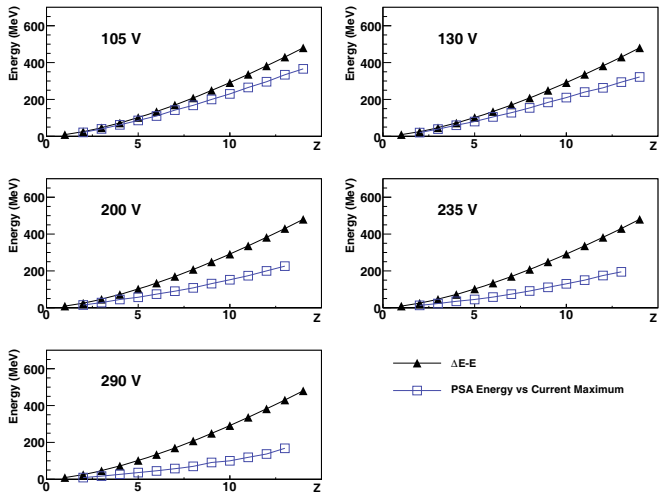

Fig. 25. (Colour on-line) Charge identification thresholds estimated from visual inspection of energy *versus* current maximum correlations (empty squares). Thresholds for the ΔE-E techniques are also shown as filled triangles for 300 μm silicon thickness. From [41,42].

From this test we learn that, by under-biasing the first stage of a ΔE-E telescope, one could still lower the energy thresholds for PSA isotopic identification, palliating thus an eventually poor doping uniformity.

6.2 Single Chip Telescope (SCT)

Part of the effort in designing FAZIA was devoted to reducing the complexity and cost of the apparatus. To this aim, one could use the second silicon detector both as a ΔE detector and as a photo-diode for the reading out of the CsI(Tl) scintillation light. This solution, called "Single Chip Telescope" (SCT), was first proposed and tested twenty years ago [43,44]. When applied to an array covering a large solid angle, the main advantage of the SCT configuration is the reduced number of FEE channels with respect to a standard ΔE-E telescope (a factor of two for a Si-CsI(Tl) telescope), allowing for less crowded front end, lower power dissipation in vacuum and reduction in cost. As a disadvantage, a dedicated and somewhat critical signal-analysis procedure is needed to extract from a unique signal the necessary information for charge and mass identification. In the FAZIA implementation of the SCT, signals have been digitized (using sampling boards developed within the Collaboration) and stored for offline analysis. In our test, the SCT was part of a Si-Si-CsI(Tl) telescope (the TeleC of ref. [15]): the SCT constitutes the second and third stage of the telescope while the first silicon detector acts as a standard "first layer" detector In order to get better particle identification from PSA, all silicon detectors were mounted with the ohmic rear side facing the target so that particles enter the detector from

the low field side. A 20 nm thick aluminum layer was deposited on the ohmic side, while on the junction side only a very thin silicon dioxide layer is present. The junction side is thus sensitive to visible light photons with almost unit quantum efficiency, a mandatory feature for employing the detector as a regular silicon photo-diode. A standard Si-Si-CsI(Tl) telescope (TeleD) was used as a reference to compare SCT identification to that obtained with standard photo-diode readout of the CsI(Tl). We refer to ref. [45] for details.

During the analysis, the digitized SCT signal is duplicated and the two copies are processed via different digital shapers (semi-Gaussian) with different time constants. In the following, the shaper with the shorter time constant will be called "short" shaper, the other "long" shaper.

Let us call S and L the peak amplitudes of the short- and long-shaped signals, respectively. In this work, the short shaper has a peaking time $T_S = 700\,\text{ns}$ and the long shaper has a peaking time $T_L = 8\,\mu\text{s}$. A digital pole-zero cancellation of the exponential decay of the PACI preamplifier is performed on all signals before applying the shaping filters.

It is found (see [45]) that the ΔE (energy loss in the second silicon detector) and E_{RES} (residual energy in the CsI(Tl) crystal) information (in arbitrary units) can be obtained as follows:

$$\Delta E \propto S - K_L L \qquad E_{\text{RES}} \propto L - K_S S. \tag{4}$$

The K_L and K_S coefficients can be adjusted, by trials and errors, until the events with no scintillation light become parallel to the ordinate axis and those with no direct ionization in silicon (*i.e.* gamma and neutrons interacting with the CsI only) become parallel to the abscissa. As a result of such an adjustment, ΔE *versus* E_{RES} plots are obtained. Spurious events associated with particles stopped in silicon will be present in the plots. To avoid them, some criteria, based on PSA, must be devised, see [45] for details.

Using the adopted selection criteria, one can produce the "cleaned up" ΔE-E_{RES} correlations shown in figs. 26 and 27, where ΔE and E_{RES} are calculated using $K_L = 0.4$ and $K_S = 1.02$. Element resolution is obtained in the whole range allowed by the FEE saturation amplitude (up to $Z \approx 13$). A reasonable mass separation is achieved for LCP's and low-Z IMF's up to Be. However, only marginal mass resolution is achieved for boron and carbon isotopes: different masses can be recognized only in a small energy range. No mass resolution is achieved for $Z > 6$.

The ΔE-E_{RES} correlations have been subsequently linearized, extracting a particle identification (PID) parameter to quantitatively estimate the isotopic resolution.

In order to check how the particle identification degrades with energy, in fig. 28 the FoM for different isotope pairs is plotted as a function of the estimated particle energy, E_{INC}, at the entrance of the silicon of the SCT. To do so, first PID spectra have been obtained for adjacent intervals of light output of the CsI(Tl) and the FoM values of various isotope pairs have been calculated in each slice. Then for each slice and isotope pair (*i.e.* for each point in fig. 28) the average E_{INC} value of the lower-mass isotope has been estimated from the ΔE measured by Si1 and from energy loss tables [46].

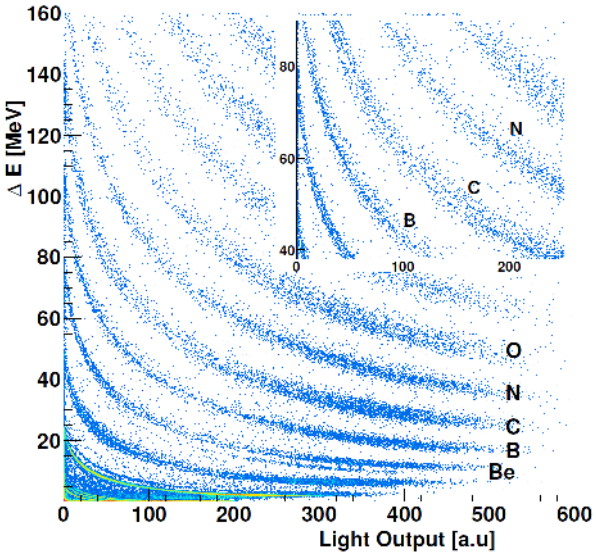

Fig. 26. (Colour on-line) Reconstructed ΔE (in MeV) *versus* CsI(Tl) light output (a.u.) for IMF's. In the inset, an expanded view of the region where Carbon isotopes are better resolved is shown. Counts are plotted on a logarithmic scale. From [45].

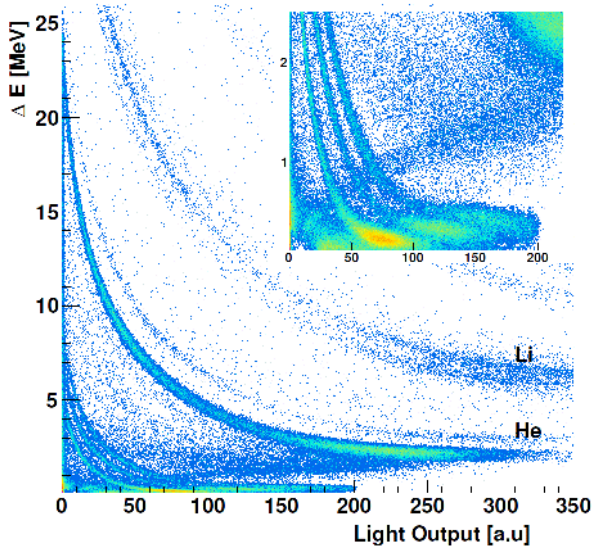

Fig. 27. (Colour on-line) Reconstructed ΔE (in MeV) *versus* CsI(Tl) light output (a.u.) for LCP's. In the inset, an expanded view of highest energy hydrogen isotopes is shown. Counts are plotted on a logarithmic scale. From [45].

The FoM values for LCP's show that a comparable performance can be obtained from the standard telescope and the SCT. For IMF's, on the contrary, the SCT is not as good as the standard telescope, especially at low energies.

In order to evaluate the effect of the SCT reconstruction procedure on isotopic identification, we have built "SCT-like" signals from the Si2 and CsI(Tl) signals of TeleD, see [45] for details. Signals obtained in such a way

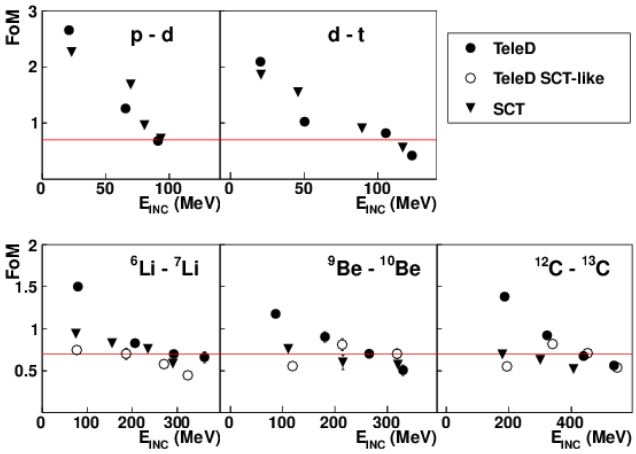

Fig. 28. FoM values for different isotope pairs as a function of the average incident energy $E_{\rm INC}$ of the first isotope (p, d, ^{6}Li, ^{9}Be, ^{12}C, respectively) before entering the SCT. The results are for the SCT (triangles) and for the standard telescope, TeleD (dots). For the latter, Si and CsI(Tl) signals have been treated separately (full dots) or mixed in a single composite signal (open dots). The incident energy is calculated on the basis of the ΔE energy measured by the preceeding first silicon. Each point corresponds to an interval of CsI(Tl) Light Output values. The 0.7 limit is evidenced by the horizontal (red) line. Error bars refer only to statistical uncertainties. From [45].

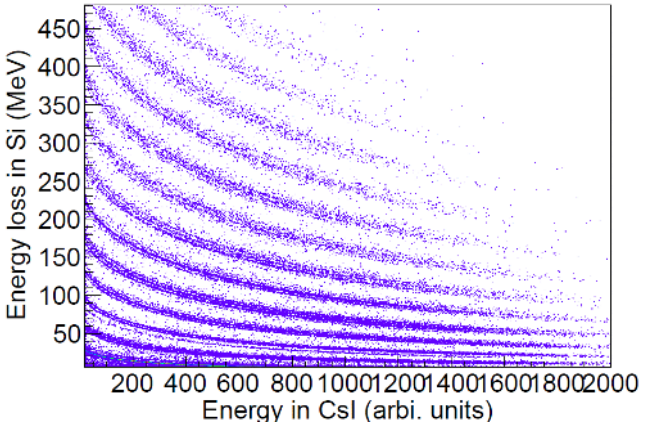

Fig. 29. (Colour on-line) ΔE-E plot of four p-side readout strips *vs.* CsI(Tl).

have been analyzed using the same reconstruction procedure as for the actual SCT signals. ΔE-$E_{\rm RES}$ correlations similar to those of figs. 26 and 27 have been produced and linearized. The FoM for neighbouring isotopes is plotted in fig. 28 (open circles). Comparing the FoM values obtained for TeleD with the two methods (full and open circles in fig. 28), we find that the reconstruction procedure worsens the resolution particularly at low energy. One could then attribute the worse FoM values obtained at the lowest energies for the SCT, with respect to the TeleD standard, to the need to extract the information from a single signal. The isotopic resolution is influenced, for high $E_{\rm RES}$, more by the resolution in ΔE than in $E_{\rm RES}$. In a Si-CsI(Tl) telescope, the $E_{\rm RES}$ measurement is certainly more affected by statistical fluctuations than the ΔE measurement, due to the lower number of carriers. In fact, taking into account light collection efficiency, scintillation photons in CsI(Tl) have an energy cost at least one order of magnitude larger than electron-hole pairs in Si. When ΔE is obtained from a single signal combining the ΔE and $E_{\rm RES}$ information, the larger fluctuations in $E_{\rm RES}$ can negatively affect the reconstructed ΔE value, thus spoiling the isotopic resolution with respect to a standard telescope where ΔE and $E_{\rm RES}$ are treated separately. Other details on this behavior and its possible explanations can be found in ref. [45].

6.3 Double-sided silicon strip detector

In the scientific program of the FAZIA Collaboration a specific development concerning double-sided silicon strip detectors (DSSSD) has been carried out. The good angular resolution of DSSSD allows to study correlation functions which are a powerful experimental tool to investigate not only the dynamics of heavy-ion collisions but also the spectroscopy of exotic nuclei [47–54]. The granularity of the FAZIA detector, of about $\Delta\vartheta \sim 1^{o}$, will be improved in some specific part of the solid angle by using Si-strip detectors as first detection layer, thus allowing an angular resolution of about $\Delta\vartheta \sim 0.1\,^{\circ}$. This angular resolution improvement will permit to study space-time features of nuclear reaction mechanisms [55] and exotic spectroscopic features, such as molecular states and clusterings [56–58].

A $50 \times 50\,{\rm mm}^2$ double-sided n-TD silicon strip detector, 2×16 strips, has been tested in the reverse-mounting configuration. It was designed by Micron Semiconductor company and silicon wafers were provided by TOPSIL. The thickness of the detector is $500\,\mu$m. In front of the Si-strip, a $300\,\mu$m n-TD silicon detector (Si1) measured the energy loss. This allowed to identify the particles stopped in the Si-strip detector by the ΔE-E method and to check the DSSSD PSA-identification. Behind the Si-strip a CsI detector measured the residual energy of the particles punching through the Si-strip detector and could be used as a veto. The Si-strip detector was placed 1 m away from the target at a polar angle of about $10\,^{\circ}$. Only 7 strips (3 on the ohmic side and 4 on the p-side) out of 32 were considered for these measurements because of the limited number of electronic channels available. The used PACI preamplifiers [11] had two outputs for charge and current signals with a gain of 3.6 mV/MeV and 3000 V/A, respectively. They were connected directly to the Florence cards [17] (125 Ms/s and 12 bit). The beam for this experiment was Kr at $E = 35$ MeV/nucleon.

The identification obtained from the ΔE-E plot (energy loss in Si1 *versus* the residual energy collected with p-side readout strips) gives excellent results, comparable to those of fig. 7. This occurs because the identification quality mainly depends on the signal of the first n-TD detector. The ΔE-E bi-dimensional plot of p-side readout strips as a function of CsI light output is presented in fig. 29. In this case the Si-strip detector gives isotopic identification of the particles up to the maximum charge ($Z = 14$) detected in the CsI detector. The isotopic resolution is comparable to

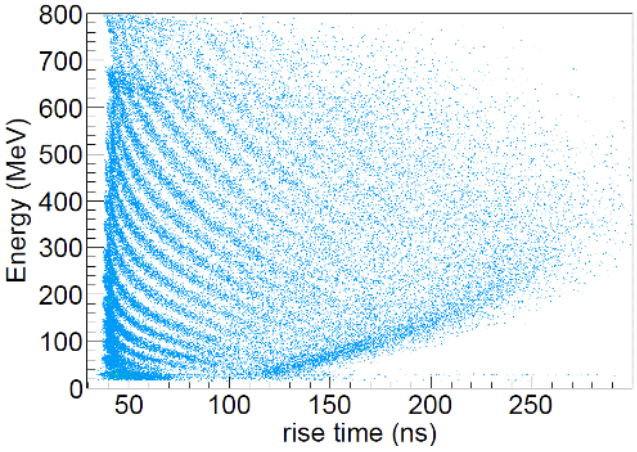

Fig. 30. (Colour on-line) PSA identification for the three ohmic-side readouts: energy *vs.* charge rise-time.

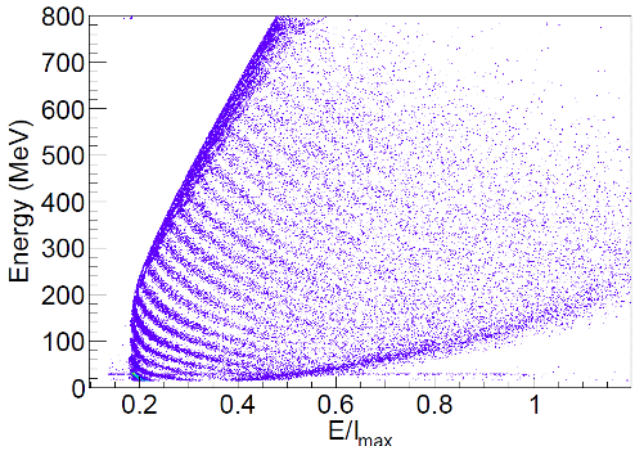

Fig. 31. (Colour on-line) PSA identification for the three ohmic-side readout: Energy as a function of the ratio $E/I_{\max}$.

the one provided by the mono-cell silicon detector. Similar results are obtained with ohmic side readout of Si-strip detector. We then tested two PSA methods to identify particles stopped in the strip-detector. The charge signal rise-time as a function of the energy of the fragments stopped in the Si-strip detector was examined for both the p-side (4 strips) and the ohmic-side (3 strips) readouts.

Figure 30 shows the Z identification obtained from the 3 strips of the ohmic side readout. A better resolution is obtained with the ratio of the energy (E) divided by the current signal maximum ($I_{\max}$) of the detected ions, as shown in fig. 31. Results of the same quality are obtained for the p-side readouts (not shown). The resolution is similar to that obtained with the FAZIA mono-cell detectors. This demonstrates that it is not necessary to digitize signals from both sides of the Si-strip detector in order to achieve a good PSA identification.

A specific problem with Si-strip detectors comes from the "inter-strip" entering particles: their energy is shared between two adjacent strips and to reconstruct it a common practice is to sum up both contributions. In the previous figures, inter-strip events were excluded from the analysis. Different methods were tested to identify these inter-strip particles by PSA. The rise-times associated with the adjacent strips cannot be easily combined. The best method we found is the use of the variable $E/I_{\max}$ ratio in the form $(E_i + E_{i+1})/(I^i_{\max} + I^{(i+1)}_{\max})$, where i and $i+1$ denote two adjacent strips. A satisfactory identification of fragments is obtained due to the fact that the original current signal maximum seems to be recovered by combining the current signals of two adjacent strips.

6.4 Ion identification using the time-of-flight technique

As it has been stressed, the implementation of both ΔE-E and PSA techniques permits to significantly extend the identification range in terms of Z and A and energy of detected ions. However the very low energy region is not covered and this happens when ions are stopped in the very first tens of micron of the detector. For this reason the FAZIA Collaboration from the very beginning decided to study the timing characteristics of the detectors also in view of possible implementation of the ToF technique. Actually this comes out "for free" because the PSA technique is intrinsically based on timing performances when the identification is obtained from the charge *vs.* rise-time correlation, one of the two approaches used by FAZIA. As a matter of fact the main limitation to timing performances derives from a possible dependence of the signal shape on the impact point: in order to keep this effect at its smallest value the sheet resistance of the detectors has to be kept as low as possible. A 30 nm aluminum layer deposited on the front face of the detectors is sufficient to keep the sheet resistance to a few ohm value [59]. In order to test the limit of timing, time resolution has been studied with laboratory tests. These tests were performed by using a sub-ns light pulse obtained by Q-switch laser and measuring the FWHM resolution for the time coincidence of two FAZIA silicon detectors illuminated by the light flash from diffused laser pulses. The obtained FWHM [42] is smaller than 100 ps, in agreement with earlier results obtained at the very beginning of the R&D activity in FAZIA [25]. On the basis of this result, it is clear that the limitation to ToF identification quality in a real experiment will depend on the pulsed beam quality, typically not better than 1 ns. Therefore the actual exploitation of the ToF technique will be decided on the basis of the availability of a sufficient beam pulse resolution (or an alternative method) and on the available flight path.

7 Conclusion

Thanks to the excellent identification performances of the FAZIA protopypes described in this paper, the data acquired during one of the last in-beam runs for testing the detectors could be already used for investigating some aspects of isospin physics. This resulted in two papers that addressed the issues of isospin transport [60] and odd-even staggering in N and Z [61] by studying the isotopic resolved light projectile fragments produced in the interaction with targets of different N/Z.

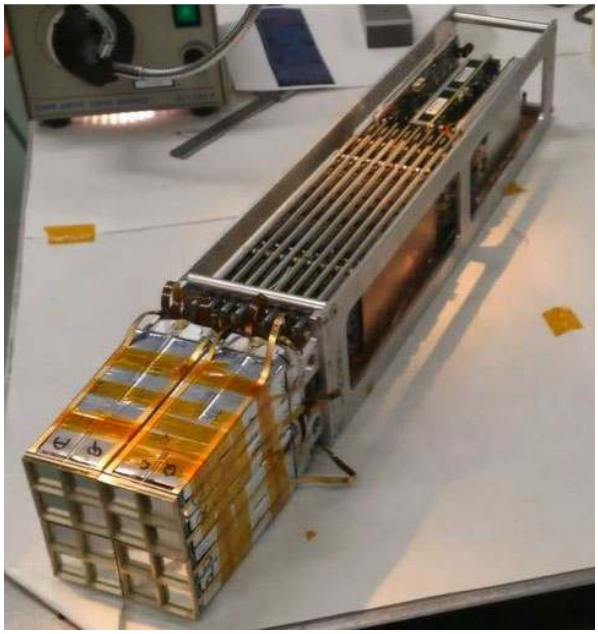

Fig. 32. (Colour on-line) One block of FAZIA with embedded electronics.

After the R&D phase described in this article, a Memorandum of Understanding has been signed to construct and operate a demonstrator of a future FAZIA array. The agreement was signed by France, Italy, Poland and Romania.

The demonstrator under construction will consist of 12 blocks. Each block contains 16 detection elements. The detection element of FAZIA consists of a $20\times20\,\mathrm{mm}^2$ Si-Si-CsI(Tl) telescope, implemented in such a way as to exploit the standard ΔE-E identification technique for particles punching through the first silicon and the more sophisticated approach of PSA for particles stopped in it. The detector will be implemented with a fully digital approach and will follow the FAZIA recipes described in this article. A photo of one block is presented in fig. 32. It is seen that the front-end electronics is located as close as possible to the detectors. One optical fibre is used to extract the data towards the acquisition system. For the demonstrator, charge and current signals will be digitized. For the future multi-detector a choice will be made. Two gains are used for the first stage in order to get isotopic identification by PSA. The digitization characteristics are:

- Stage 1 (300 μm silicon detector):
  - Charge: 250 Ms/s 14 bit (250 MeV full scale);
  - Charge: 100 Ms/s 14 bit (4 GeV full scale);
  - Current: 250 Ms/s 14 bit .
- Stage 2 (500 μm silicon detector):
  - Charge: 100 Ms/s 14 bit (4 GeV full scale);
  - Current: 250 Ms/s 14 bit.
- Stage 3 (10 cm CsI(Tl) + photo-diode):
  - Charge: 100 Ms/s 14 bit (4 GeV silicon-equivalent full scale).

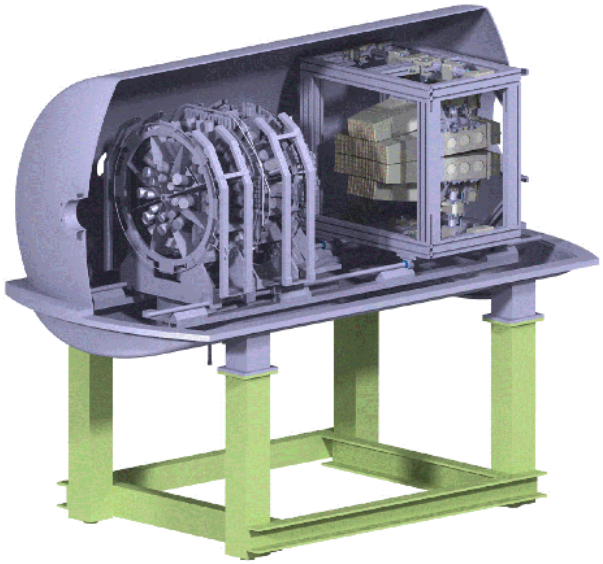

Fig. 33. (Colour on-line) FAZIA demonstrator coupled to INDRA multi-detector.

FAZIA is designed in such a way to be easily movable and coupled to other apparatuses in order to permit a very rich scientific program exploiting various stable and radioactive beam facilities, with complementary campaigns at GANIL (SPIRAL2), LNL (SPES), LNS (FRIBS) and EURISOL. Very soon the demonstrator will be coupled to the INDRA array at GANIL (fig. 33) for physics experiments. Approved experiments will also be performed at LNS using the FAZIA demonstrator.

We would like to thank the staff of LNS, LNL and GANIL for providing very good quality beams. Thanks are also due to N. Zorzi of FBK (Trento) for cooperative support in detector development. This work has been supported by the Agence Nationale de la Recherche under Grant number ANR-05-BLAN-0373-01 and grants of Italian Ministry of Education, University and Research under contract PRIN 2010-2011. The research leading to these results has received funding from the European Union Seventh Framework Program FP7 (2007-2013) under Grant Agreement no262010 - ENSAR and E.U. SPIRAL2 preparatory phase. We acknowledge support by INFN-Italy, IN2P3/CNRS-France, GANIL-France, the Romanian Ministry of Education and Research (Project PN 09 37 01 05) and the Foundation for Polish Science MPD program co-financed by the European Union within the European Regional Development Fund.

References

1. G. Paush *et al.*, IEEE Trans. Nucl. Sci. **44**, 1040 (1997).
2. M. Mutterer *et al.*, IEEE Trans. Nucl. Sci. **47**, 756 (2000).
3. C.A.J. Ammerlaan *et al.*, Nucl. Instrum. Methods A **22**, 189 (1963).
4. J.B.A. England *et al.*, Nucl. Instrum. Methods A **280**, 291 (1989).
5. G. Paush *et al.*, Nucl. Instrum. Methods A **337**, 337 (1994).
6. G. Paush *et al.*, IEEE Trans. Nucl. Sci. **43**, 1097 (1996).

7. J. Pouthas *et al.*, Nucl. Instrum. Methods A **357**, 418 (1995).
8. A. Pagano *et al.*, Nucl. Phys. A **734**, 504 (2004).
9. M. Bruno *et al.*, Eur. Phys. J. A **49**, 128 (2013).
10. M. Pârlog *et al.*, in *Proceedings of the IWM 2003, International workshop on multifragmentation and related topics* (GANIL, Caen, 2004).
11. H. Hamrita *et al.*, Nucl. Instrum. Methods A **531**, 607 (2004).
12. L. Bardelli *et al.*, in *Proceedings of the International Workshop on Multifragmentation IWM2005*, edited by R. Bougault, A. Pagano, S. Pirrone, M.-F. Rivet, F. Rizzo (SIF, Bologna, 2005) ISBN 88-7438-029-1.
13. M. Pârlog *et al.*, Nucl. Instrum. Methods A **613**, 290 (2010).
14. Z. Sosin *et al.*, Nucl. Instrum. Methods A **693**, 170 (2012).
15. S. Carboni *et al.*, Nucl. Instrum. Methods A **664**, 251 (2012).
16. W. von Ammon *et al.*, Nucl. Instrum. Methods B **63**, 95 (1992).
17. G. Pasquali *et al.*, Nucl. Instrum. Methods A **570**, 126 (2007).
18. L. Bardelli *et al.*, Nucl. Instrum. Methods A **654**, 272 (2011).
19. L. Bardelli *et al.*, Nucl. Instrum. Methods A **605**, 353 (2009).
20. L. Bardelli *et al.*, Nucl. Instrum. Methods A **602**, 501 (2009).
21. S. Barlini, *et al.*, Nucl. Instrum. Methods A **600**, 644 (2009).
22. N. Le Neindre *et al.*, Nucl. Instrum. Methods A **701**, 145 (2013).
23. F.Z. Henari *et al.*, Nucl. Instrum. Methods A **288**, 439 (1990).
24. H.A. Rijken *et al.*, IEEE Trans. Nucl. Sci. **40**, 349 (1993).
25. L. Bardelli *et al.*, Nucl. Instrum. Methods A **521**, 480 (2004).
26. W. Seibt *et al.*, Nucl. Instrum. Methods A **113**, 317 (1973).
27. G. Paush *et al.*, Nucl. Instrum. Methods A **365**, 176 (1995).
28. W.M. Gibson *et al.*, Phys. Rev. Lett. **15**, 3 (6)0)1965.
29. B.R. Appleton *et al.*, Phys. Rev. **161**, 330 (1967).
30. J.J. Grob *et al.*, Phys. Rev. B **11**, 3273 (1975).
31. A.A. Alexandrov *et al.*, Nucl. Instrum. Methods A **312**, 542 (1992).
32. G. Poggi *et al.*, Nucl. Instrum. Methods B **119**, 375 (1996).
33. L. Bardelli *et al.*, Nucl. Instrum. Methods A **560**, 517 (2006).
34. R.A. Winyard *et al.*, Nucl. Instrum. Methods **95**, 141 (1971).
35. R.J. Charity *et al.*, Nucl. Phys. A **476**, 516 (1988).
36. S. Barlini *et al.*, Nucl. Instrum. Methods A **707**, 89 (2013).
37. M. Alderighi *et al.*, IEEE Trans. Nucl. Sci. **53**, 279 (2006).
38. A. Alberigi Quaranta *et al.*, IEEE Trans. Nucl. Sci. **15**, 373 (1968).
39. I. Kano, Nucl. Instrum. Methods A **353**, 93 (1994).
40. H. Hamrita *et al.*, Nucl. Instrum. Methods A **642**, 59 (2011).
41. G. Pasquali *et al.*submitted to Eur. Phys. J. A, arXiv:1402.4943 [physics.ins-det].
42. G. Pastore, Master Thesis, University of Florence (2013).
43. G. Pasquali *et al.*, Nucl. Instrum. Methods A **301**, 101 (1991).
44. G. Prete *et al.*, Nucl. Instrum. Methods A **315**, 109 (1992).
45. G. Pasquali *et al.*, Eur. Phys. J. A **48**, 158 (2012).
46. F. Hubert *et al.*, At. Data Nucl. Data Tables **46**, 1 (1990).
47. Y. Blumenfeld *et al.*, Nucl. Instrum. Methods A **421**, 471 (1999).
48. B. Davin *et al.*, Nucl. Instrum. Methods A **473**, 302 (2001).
49. E. Pollaco *et al.*, Eur. Phys. J. A **25**, 287 (2005).
50. M.S. Wallace *et al.*, Nucl. Instrum. Methods A **583**, 302 (2007).
51. M. Labiche *et al.*, Nucl. Instrum. Methods A **614**, 439 (2010).
52. G. Verde *et al.*, J. Phys. Conf. Ser. **420**, 012158 (2013).
53. D. Torresi *et al.*, Nucl. Instrum. Methods A **713**, 11 (2013).
54. B. Davin *et al.*, Nucl. Instrum. Methods B **317**, 661 (2013).
55. G. Verde *et al.*, Eur. Phys. J. A **30**, 81 (2006).
56. R. Charity *et al.*, Phys. Rev. C **52**, 3126 (1995).
57. W. Tan *et al.*, Phys. Rev. C **69**, 061304 (2004).
58. F. Grenier *et al.*, Nucl. Phys. A **811**, 126 (2008).
59. S. Valdrè, Degree Thesis, University of Florence (2009).
60. S. Barlini *et al.*, Phys. Rev. C **87**, 054607 (2013).
61. S. Piantelli *et al.*, Phys. Rev. C **88**, 064607 (2013).